DESIGN AND CONSTRUCTION OF THE FUNDAMENTAL TOOLS FOR SINGLE ATOM EXPERIMENTS

A Thesis

by

Mehmet Öncü

Submitted to the
Graduate School of Sciences and Engineering
In Partial Fulfillment of the Requirements for
the Degree of

Masters of Science

in the
Department of Electrical and Electronics Engineering

Özyeğin University
July 2022

DESIGN AND CONSTRUCTION OF THE FUNDAMENTAL TOOLS FOR SINGLE ATOM EXPERIMENTS

Approved by:

Assistant Professor Kadir Durak, Advisor
Department of Electrical and Electronics Engineering
Özyeğin University

Professor Özgür E. Müstecaplıoğlu
Department of Physics
Koç University

Professor Fatih Uğurdağ
Department of Electrical and Electronics Engineering
Özyeğin University

Date Approved: 05/07/2022

To those I love

ABSTRACT

Neutral atoms are one of the most promising systems for quantum information and quantum engineering, in general. Full and efficient control over cold atoms and their interactions with light has been challenging and exciting task especially for quantum information and engineering. These systems now can be integrated successfully to the applications like implementation of quantum internet, simulation and experiments involving nonlinear single-photons.

Rubidium atoms provide a playground for atomic physics experiments and applications since it has accessible atomic transition and a readily available two-level system. In order to manipulate single ^{87}Rb atoms, experimental tools should be meticulously prepared. Since the atomic quantum states are delicate and fragile, their interaction with light should be handled with care. For the manipulation of these atoms, low linewidth stable laser systems should be constructed to provide an efficient and effective solution. To achieve the required stability, the external-cavity diode laser (ECDL) and frequency modulation (FM) spectroscopy setups are constructed to obtain the low-linewidth, high-stability laser source. Alongside the laser setup, an ultra-high vacuum (UHV) setup is constructed and up to a 2.5×10^{-10} mbar vacuum level is obtained. To reach ultra-high vacuum levels, additional baking is performed and Rb atom source is mounted to be readily used. UHV setup is required to minimize the background collisions and decrease the environmental disturbances from the targeted atomic system. Lastly, optical cavities that will be used to manipulate single atoms are computationally studied in this thesis. Although the strong focusing cavities are used to achieve high coupling strength, they come with several disadvantages. Since they are on the edge of the stability diagram, higher-order mode excitation is dominant

for the cases where focusing strength is the highest. Therefore, knowing the mode structure is important for those regimes to have a complete understanding of these devices. Together with laser and UHV setups, optical cavities are the complementary part of most single-atom experiments.

ÖZETÇE

Nötr atomlar, genel olarak kuantum bilişim ve kuantum mühendisliği için en umut verici sistemlerden biridir. Soğuk atomlar ve bunların ışıkla etkileşimleri üzerinde tam ve verimli kontrol sağlanması, özellikle kuantum bilişim ve mühendisliği için zorlu ve heyecan verici bir görev olmuştur. Bu sistemler artık kuantum internet uygulamaları, kuantum simülasyon ve doğrusal olmayan tek fotonları içeren deneyler gibi uygulamalara başarıyla entegre edilebilir. Rubidyum atomları, erişilebilir atomik geçişe ve hazır iki seviyeli bir sisteme sahip olmaları sebebiyle, atom fiziği deneyleri ve uygulamaları için bir "oyun alanı" sağlar. Atomik kuantum durumları hassas ve kırılgan olduğundan, ışıkla etkileşimleri dikkatle ele alınmalıdır ve bu sebeple ^{87}Rb atomlarını manipüle etmek için kullanılacak olan deneysel araçlar titizlikle hazırlanmalıdır. Bu atomların manipülasyonunda, verimli ve etkili bir çözüm sağlamak için düşük bant genişliğine sahip stabil lazer sistemleri kurulmalıdır. Gerekli kararlılığı elde etmek için, dış ayna lazer sistemi (ECDL) ve frekans modülasyonlu (FM) spektroskopi düzenekleri oluşturulmuştur. Lazer kurulumunun yanı sıra ultra yüksek vakum düzeneği (UHV) kurulumu yapılmış ve 2.5×10^{-10} mbar basınç değeri elde edilmiştir. Ultra yüksek vakum seviyelerine ulaşmak için vakum düzeneğini ısıtılması gerektedir. Isıtma işleminin tamalanmasıyla birlikte rubidyum kaynağı olarak kullanılacak Rb dağıtıcıları düzeneğe entegre edilerek bağlanmış ve hazır duruma getirilmiştir. Rb atomlarının atmosfer maruz kaldığı çarpışmaları minimuma indirmek için UHV düzeneği kurulumu son derece önem arz etmektedir. Son olarak, bu tezde tek atomları manipüle etmek için kullanılacak optik kaviteler incelenmiştir. Yüksek odaklı optik kaviteler, yüksek eşlenme gücü elde etmek için kullanılsa da, çeşitli dezavantajları beraberinde getirirler. Stabilite diyagramının kenarında oldukları için, odaklanma kuvvetinin en yüksek

olduğu durumlarda daha yüksek mertebeden mod uyarımı dominant hale gelmektedir. Bu nedenle, yüksek odaklama gücüne sahip optik kavitelerin mod yapısını bilmek, bu cihazları tam olarak anlamak için son derece önem arz etmektedir. Lazer ve UHV düzeneği kurulumlarıyla birlikte optik kaviteler, tek-atom deneylerinin tamamlayıcı parçalarıdırlar.

ACKNOWLEDGEMENTS

First and foremost I would like to thank Dr. Kadir Durak for his countless support. I would like to express my special thanks to Asu for her contributions to the project and her friendship. My appreciation to all cold atom members and Dr. Özgür E. Müstecaplıoğlu for their contributions and help throughout my masters. I am grateful to all Quantum Optics Lab members for their countless support, especially Hashir Kuniyil for his friendship and enjoyable tea discussions. I would like to thank Dr. Bora Işıldak for his entertaining and informative discussions. Thanks to my family for their constant support and help. Lastly, I am grateful to my wife for always being there for me.

The researches in this thesis are supported by the Scientific and Technological Research Council of Turkey (TUBITAK) with the career grant no: 119F200.

TABLE OF CONTENTS

LIST OF FIGURES

CHAPTER I

INTRODUCTION

Understanding the interaction of the matter with the light has been a real challenge for too long. It even constitutes a basis for the fundamental understanding of nature itself. Throughout the course of history, our experimental tools become sophisticated and we have reached the unprecedented accuracy and precision that has never been achieved. The most important milestone for these types of experiments is the invention of the laser in 1960 [6]. With the invention of the laser, we have reached a whole new level in the control of the interaction between matter and electromagnetic radiation, and experimental proposals and verifications come one after another. Proposal of laser cooling of neutral atoms in 1975 [7] and experimental demonstrations [8, 9, 10, 11] proved that those types of experiments should be carefully handled. Environmental interactions should be reduced and the system of interest should be isolated and well-prepared.

Isolated and closed system definition is different in quantum mechanics than it is for example in thermodynamics. You can isolate a container of gas and control its macroscopic features like pressure and temperature. However, you cannot isolate a so-called quantum system from its environment and you cannot easily and deterministically manipulate its state features as can be done in thermodynamics. Quantum systems are fragile and they are constantly interacting with their neighboring environmental objects. For that reason, they must be cooled to reduce the effect of their constant motion, and have minimum amount of environmental interaction. de Broglie thermal wavelength shows that to observe the quantum effects in the objects that have a greater mass, the temperature should be lower. To be more precise we

need to observe the atoms when they are not moving and they are isolated from the rest of the universe.

In the case of atoms, laser cooling provides one of the solutions for the low enough temperatures. Laser cooling takes advantage of the fact that photons carry momentum, unlike their masses. Basically, the group of atoms are kicked with photons and are confined in a certain position. When the group of atoms is slowed down, it automatically means that they are cold, because the temperature is average kinetic energy of the each constituent of the target system. Using laser cooling techniques, it is possible to reach the temperatures from micro Kelvins to nano Kelvins [12, 13, 14, 15]. Cold atoms provide one of the most controllable and precise playgrounds to study fundamental phenomena like light - matter interactions, as well as the most precise engineering applications [16, 17, 18, 19, 20]. They provide even a testbed for most of the quantum computing research [21, 22, 23, 24]. One of the most important and conventional atom trapping techniques is the magneto-optical trap, which is combining the mechanical effect of the laser beam on the atoms with the magnetic field gradient provided by two opposite current coils. Atoms cooled by lasers are trapped by the force created by magnetic coils. Those coils create a position-dependent quadrupole magnetic field which acts as a restoring force for the atoms moving away from the trap center. Trapped atoms are cooled down to micro kelvin temperatures which are limited by the Doppler temperature which is the minimum temperature achieved by the Doppler cooling [25]. Micro kelvin temperature cold atoms provide important precision and accuracy for most scientific applications. In addition to laser-cooled atoms, it is possible to select a single atom by using a dipole force of the light which is called an optical tweezer technique [26]. Using single atoms, extreme light and matter phenomena can be studied. Especially, one of the most important challenges is to have a deterministic control over single atoms. To have such an unimaginable result, experimental apparatus should be carefully designed and constructed.

To have precise atomic control, lasers should be pre-aligned and pre-prepared. Low-linewidth frequency-locked lasers are a must for those types of experiments. Preparing such a laser required expertise for a few different areas. To have a low linewidth laser, an external-cavity diode-laser (ECDL) method is used. This method requires at least one additional optical element to a simple diode laser to have feedback for increased wavelength selection. The frequency of the ECDL output should be stabilized by having a feedback loop from the additional optics and electronics. Several methods can be used to lock the frequency of the laser to a certain frequency value. FM Spectroscopy method is one of the widely used and conventional ways to lock the frequency of a laser. In this setup frequency of the laser is stabilized to a specific atomic transition and after that its frequency is shifted to the desired frequency [27, 28]. The same method can also be implemented with the optical cavities used as a frequency reference which is called a Pound-Drever-Hall (PDH) method [29].

In addition to the well-prepared lasers, one of the other most important challenges is to decrease the environmental interaction of the target atoms. As specified above, quantum objects tend to interact with the environmental background especially other particles. Additional collisions with the atmospheric molecules make it impossible to manipulate and control single atoms. To solve this issue, an ultra-high vacuum (UHV) setup is needed. UHV setups offer an easy and clean solution for most atomic physics experiments and they are indispensable. To cool and address the single atoms, lasers should be integrated into the UHV setups and the main work should be done in the chamber.

To manipulate and control single atoms coherently and deterministically, another widely used tool is optical cavities. Cavities allow us to tailor the electrical field distribution around the atoms so that their interaction strength can be increased. By doing this, photons spend more time around the atoms and they have an improved probability to interact with them. Systems include optical cavities and single atoms are

studied under the name of cavity QED and recently lots of exciting improvements takes place in this field with the start of the pioneering works [30, 31, 32]. They also have a wide range of applications from quantum networks to many-body physics [20, 33]. cavity QED applications require a strong atom-photon coupling, high precision, and sensitivity. Near-concentric cavities are the usual solutions to reach the strong coupling regime. In this thesis, optical cavities with spherical mirrors are examined, especially the ones that operate in the near-concentric regime. Some of the fundamental tools for single-atom experiments are constructed which are ECDL, FM Spectroscopy, and UHV setups. Additionally, near-concentric cavity simulations are performed in order to achieve only the desired mode of the cavity.

This thesis is organized as follows. In Chapter 2 magneto-optical trap is introduced, and underlying physical phenomena are simply explained. In Chapter 3 laser setups are explained and results are presented. In Chapter 4, the fundamentals and construction of the UHV setup are given. In Chapter 5, near-concentric cavity simulations are presented and results are discussed. Finally, in Chapter 6 thesis is concluded.

CHAPTER II

MAGNETO-OPTICAL TRAP

Photons carry momentum in a counter-intuitive way, and by using their momentum, having a mechanical impact on the atomic scale objects is possible. When the energy of the photon exactly matches the difference between the atomic energy levels, an electron is excited to the higher level by absorbing a photon which is defined as the stimulated absorption process. Absorption of the photon results in a momentum transfer to the atom in a certain direction. Since the atom is not in the stable state after the photon absorption, it loses its momentum by releasing a photon through a process called spontaneous emission. Since the spontaneous emission process is random, momentum loss due to this process averages out after a certain time leaving the effect of recoil on the atom by stimulated emission. By using this recoil effect due to the photon absorption, a group of atoms can be collected in a certain location. The force that slows down the atoms is [34],

$$\mathbf{F} = \frac{d\mathbf{p}}{dt} = \hbar \mathbf{k} \Gamma_{sc} \tag{1}$$

where Γ_{sc} is the scattering rate and can be written as,

$$\Gamma_{sc} = \frac{s_0 \Gamma/2}{1 + s_0 + (2\Delta/\Gamma)} \tag{2}$$

where Γ is the atomic spontaneous decay rate, Δ is the detuning between laser and the atomic transition, and s_0 is the saturation parameter which can be written as I/I_{sat}. Here, I is the light intensity and I_{sat} is the saturation intensity and it can be written as $I_{sat} = \pi hc\Gamma/3\lambda^3$. In the case of two counter-propagating beams, resulting force becomes,

$$\mathbf{F} = \frac{8\hbar k^2 \Delta s_0 \mathbf{v}}{\Gamma(1 + s_0 + (2\Delta/\Gamma)^2)^2} \tag{3}$$

Therefore, three pairs of counter-propagating beams are sufficient to cool the group of atoms that moves in any random direction. As one can imagine, a group of atoms, unfortunately, do not have a specific velocity value but they have a distribution of velocities. Due to the directionality of their motion, the frequency of the photon changes for each atom's reference frame which is called a Doppler shift. To address fast-moving atoms, the frequency of the light is slightly red-detuned than the targeted atomic transition. Velocity dependence can also be seen in Eq. 3. When the amount of red-detuning becomes 3-4 Γ, the recoil effect on the atom becomes maximized [35]. To efficiently locate a group of atoms in a certain position, three pairs of counter-propagating opposite polarization beams are used. Combining with the quadrupole magnetic field created by anti-Helmholtz coils (opposite current direction), it is possible to cool and trap the group of atoms to the temperatures of hundreds of μK. Anti-Helmholtz coils create a quadrupole magnetic field which is zero at the center and increase linearly to the outside of the center in all directions. Therefore required magnetic field gradient is created in a 3D configuration.

The idea of cooling atoms using lasers is proposed in 1975 and a decade later, 3D cooling and trapping experiments are reported [7, 8, 9]. A technique used to cool and trap a group of atoms by optical and magnetic forces is called the magneto-optical trap (MOT) which is now a well-known technique in the community [25]. There is a limit to the temperature of those atoms which is called a Doppler limit. It can be written as [36],

$$T_D = \frac{\hbar\Gamma}{2k_B} \tag{4}$$

where Γ is the atomic spontaneous decay rate and k_B is the Boltzmann constant. For a ^{87}Rb atom, the spontaneous decay rate is $\Gamma = 2\pi \times 6.067$ MHz which results in a Doppler limited temperature of $T_D = 145$ μK. A simple magneto-optical trap configuration

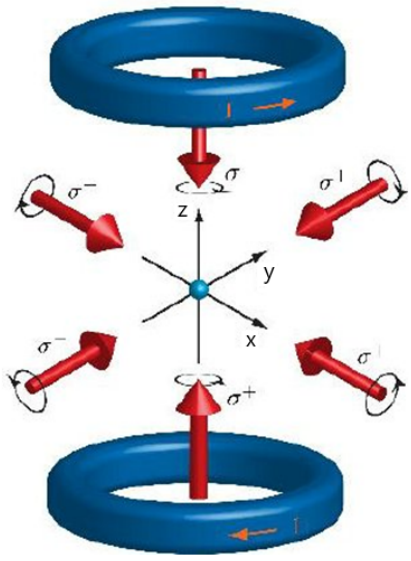

Figure 1: Magneto-optical trap is shown in detail. Three pairs of counter-propagating opposite polarization beams are sent through the group of atoms to produce an optical molasses. With the magnetic field, magneto-optical trap is completed.

can be seen in Fig. 1. Techniques that allow us to reach the temperatures below Doppler temperature are called the sub-Doppler cooling techniques which make possible temperatures down to nK levels. Some of them are Sisyphus cooling, evaporative cooling, and dark magneto-optical trap, for more information see Ref. [25, 37].

CHAPTER III

PREPARING THE LASER SETUPS

3.1 External-cavity diode-laser

Laser diodes are used in every aspect of laboratory work, since they provide high power as a compact devices. However, free-running laser diodes suffer from several drawbacks. First of all, the linewidth they offer is high which makes them insufficient to use for atomic and spectroscopic applications because the laser linewidth should be small enough to resolve the atomic transitions. Secondly, frequency control of the laser in MHz or GHz range is challenging, which makes them inappropriate for general usage. To overcome these problems, a simple but effective solution is offered; having optical feedback using additional reflective cavity elements such as diffraction gratings. This additional element constructs an external cavity and provides feedback for the laser diode. With this feedback, light bounces back and forth between the grating and the laser diode, resulting in increased wavelength selectivity. Thus, the linewidth of the laser diode becomes smaller and what is obtained is called the external cavity diode laser (ECDL) [38, 39, 40, 41]. Two different configurations are available for the ECDL in the literature; Littrow, and Littman-Metcalf configurations. In the Littrow design, the first diffraction order from the grating is sent back onto the laser diode and the zeroth-order is used as an output beam. Similarly, the Littman-Metcalf configuration also uses diffraction grating but it has an additional mirror to send the first-order beam and tune the wavelength by changing the angle of the mirror. Therefore, in the Littman-Metcalf configuration, cavity length should be taken as the distance between the grating and the mirror. While in the Littrow configuration, the external cavity length is taken as the distance between the diffraction grating and the

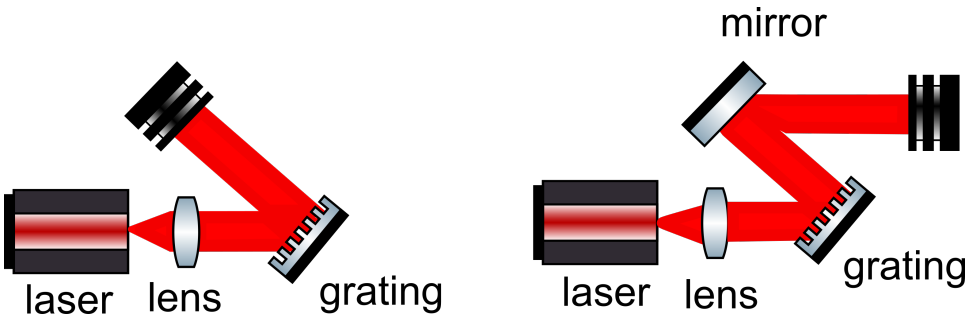

Figure 2: In the left, Littrow configuration laser cavity can be seen. In this configuration angle of the diffraction grating is changed to control the wavelength of the light. In the right, Littman-Metcalf configuration can be seen which changes the angle of the additional mirror to tune the wavelength of the light.

laser diode itself. The biggest drawback of the Littrow design is its beam direction stability. Littrow configuration ECDLs are vulnerable to external fluctuations which change the frequency of the output light thoroughly. Also, the direction of the output beam changes with the rotating diffraction grating in the Littrow design. On the other hand, the Littman-Metcalf configuration offers a stable ECDL in the exchange for the low output power. In this work, the Littrow configuration is studied, since it offers high output power, ease of control, and compact design.

Diffraction gratings take advantage of the simple diffraction phenomenon which can be explained using the classical theory of light. Diffraction equation can be written as,

$$n\lambda = d(sin\theta + sin\theta') \tag{5}$$

where n is the diffraction order, λ is the diffracted wavelength, d is the distance between two successive grating grooves, θ is the angle of the incident light with respect to the grating normal and lastly, θ' is the angle of the diffracted light with respect to the grating normal. In the Littrow design, these two angles are equal which further simplifies the equation as,

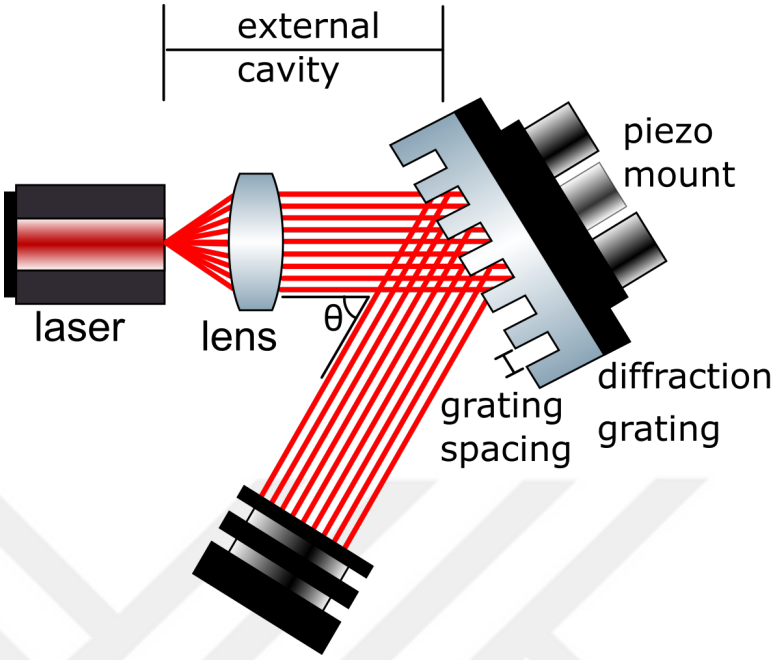

Figure 3: Basics of the Littrow configuration laser cavity can be seen from the figure. For the wavelength tuning, angle of the grating should be precisely aligned and rotated which can be done using the piezoelectric element (PZT).

$$n\lambda = 2dsin\theta. \tag{6}$$

Wavelength tuning of the ECDL for both configurations can be achieved either using the diffraction grating angles, current of the laser diode, or its temperature. In this work, wavelength tuning is done by changing the angle of the grating.

The diode laser used in this study has a typical drive current of 220 mA and a max drive current of 250 mA. The lasing threshold current is nearly 50 mA. Blazed diffraction grating which has 1200 lines/mm groove density, and is blazed at 1 μm, is used. With the groove density of 1200 lines/mm, the grating ruling distance of 833 nm is achieved. If the number is substituted into Eq. 6, it is seen that the first-order diffraction is expected at the angle of $28°$ which should be sent back to the laser diode. Typically, the first-order beams have the 20-30 % of the total power in the regular ECDL, whereas the zeroth order, which is an output beam, has 70 % of the total power [39]. How much power is sent to each order is determined by the polarization of

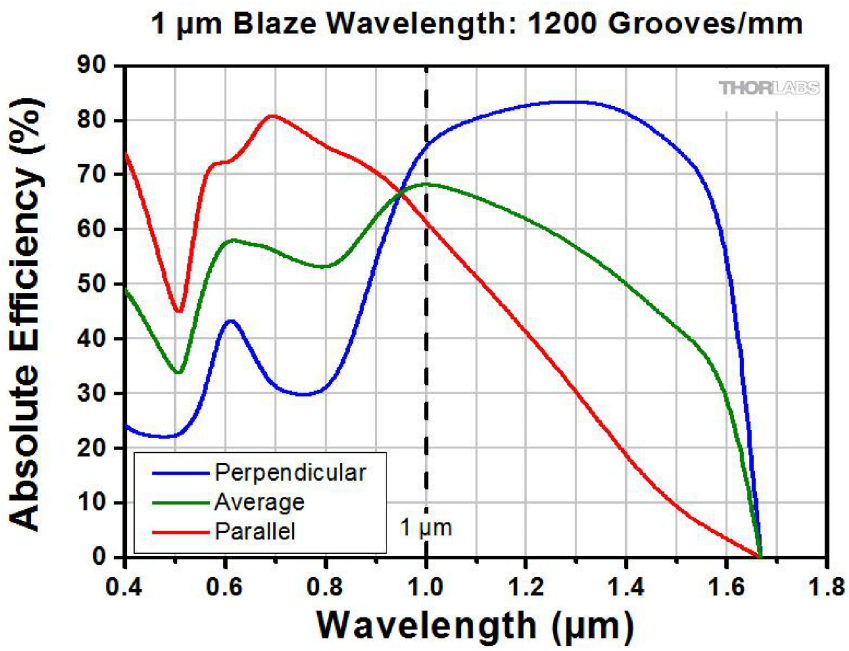

Figure 4: Efficiency curve of the diffraction grating. It can be seen that power changes with the changing polarization of light [1].

the incident light [42]. Blazed grating is used to obtain the external-cavity diode laser and these rulings in the grating are directional. How much power can be obtained for the output beam can be found by looking at the efficiency curve of the grating. For this study, the efficiency curve can be found in Fig. 4.

The efficiency curve is given for the first-order diffraction and as can be seen easily it works optimally for the blazed wavelength. Perpendicular and parallel in the efficiency curve refer to the relative conditions of the polarization of light and the direction of the grating rulings. If you say parallel, both the direction of the rulings and the polarization of light are horizontal or vertical. If perpendicular, they are in the opposite direction. By changing the polarization of the incident light, power in each order can be adjusted. This effect can be seen in Fig. 5. From the figure, four troughs and crests can be immediately seen. There are four of them since the polarization of the light becomes perpendicular after 90° angle change, and in total 360° there are four different 90° changes.

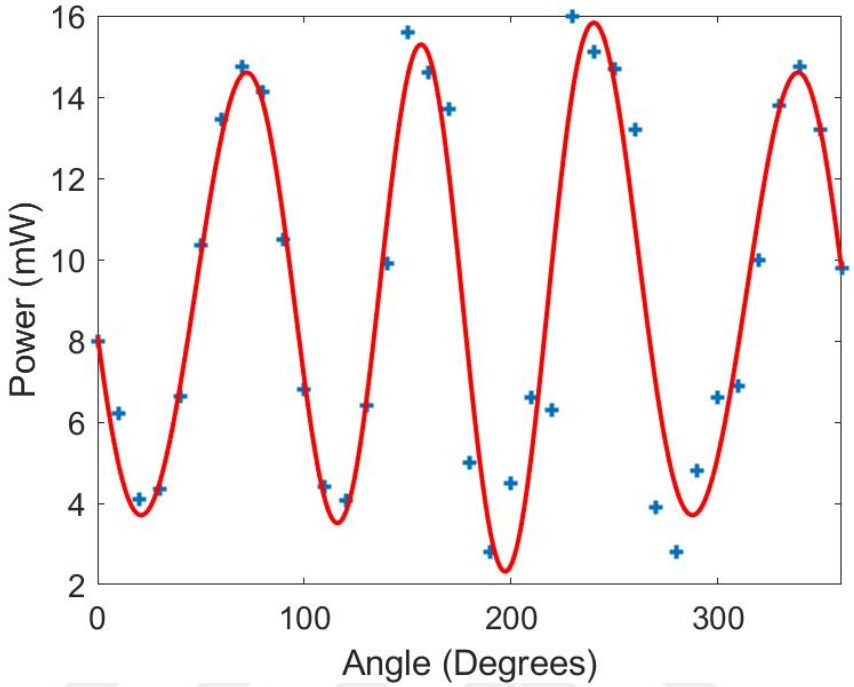

Figure 5: Change in the power of the output beam, which is the zeroth order diffracted beam, with changing polarization. As can be seen it behaves sinusoidally.

Power in the output beam becomes maximum when the direction of the polarization perfectly matches the direction of the blazed grating. On the other hand, power in the output beam is minimum when they are perfectly perpendicular. Furthermore, it should be noted that the intensity of the light is increased with the decreasing temperature [38]. Also one can measure that the lasing threshold current decreases with the decreasing temperature which has a safe temperature range of 5-50$°C$.

The geometry of the ECDL immediately results in a cavity length of approximately 20 or 30 mm [43]. Longer cavities suffer from poor stability but also offer ease of adjustability. It is measured that the output power in the zeroth-order shows periodic behavior with the changing cavity length, to be precise, it sinusoidally changes with the increasing external cavity length. In this study, the external cavity length is taken as 35 mm. For this cavity length, the free spectral range (FSR) of the external cavity can be calculated. It is known that the FSR for the air-like medium is,

$$FSR = \frac{c}{2L} \tag{7}$$

where c is the speed of light and L is the length of the cavity. If L is taken as 35 mm, the FSR for the ECDL is found as 4.29 GHz. This is the range in which laser operates without any mode-hop.

Observation of the ECDL output with a significant power might be tricky since it needs sensitive alignment. When the grating is placed, the first-order diffracted maxima should be directed back to the laser diode. While doing this, one should notice another small beam near the zeroth-order which can be barely seen. When this fainter beam exactly overlaps with the zeroth-order beam, shining in the output beam should be noticed. This means that the ECDL configuration starts to work and intensity in the output beam is increased. This intensity enhancement is more responsive to the changes in the vertical direction compared to the horizontal one when the higher diffraction orders are lined horizontally. If the setup starts to work in the ECDL configuration, one should see a decrease in the lasing threshold current of the diode laser. The amount of decrease depend on the each setup parameters, but in general, it is nearly 20-30 %. The threshold current of the laser diode that is used in this study is 50 mA which is verified experimentally.

Fig. 6 reveals that the threshold current for the laser diode is decreased by 35 %, which is more than expected. This decrease in the threshold current demonstrates that our setup starts to work in the ECDL configuration. Therefore, the laser diode needs less current to lase because of the external optical element which helps it excite more photons. The external optical element makes the stimulated emission process stronger and affects the threshold current of the laser diode.

As specified above, to control the frequency of the laser diode, the angle of the grating is controlled to adjust the external cavity length. By doing that, the frequency of the output beam can be tuned. This adjustment is so sensitive that it needs

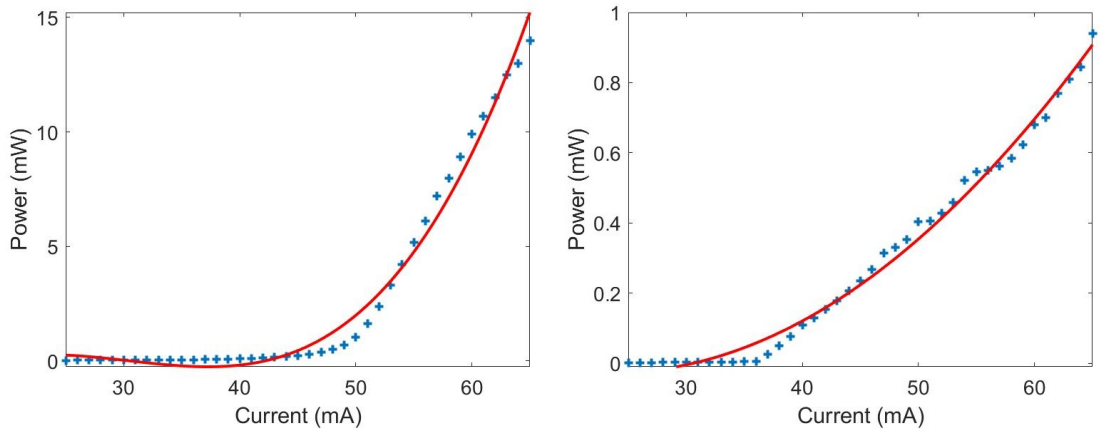

Figure 6: ECDL configuration lowers the lasing threshold current by the considerable amount. In the left, it is seen that the lasing threshold current for the free-running laser diode is nearly 35 mA. In the right, with the ECDL configuration, it can be seen that is is decreased near to the 22 mA.

a piezoelectric actuator (PZT). PZT is driven by the function generator using the triangular signal to scan the frequency range. If the angle of the grating is left just near to the ECDL angle, with the PZT one can see the shining easily when a signal is applied to the PZT.

3.1.1 Mechanical part designs and drawings

Due to the mechanical and temperature instabilities in the laser system, the laser frequency shifts very quickly and can move away from the desired value. In order to solve this problem, a few mechanical designs that are thought to be more stable are produced and used as a mount for diffraction grating and a piezoelectric actuator. Technical drawings of these designs are shown in Fig. 8. The assembled state after processing in the CNC machine is shown in Fig. 7.

Products designed for the optical product to move horizontally and vertically precisely provide the desired performance. These products are started to be used with ultra-precise screws, and the mechanical sensitivity problem is largely eliminated. The screws used have 508 pitches per inch and provide 50 µm of travel in one turn. It

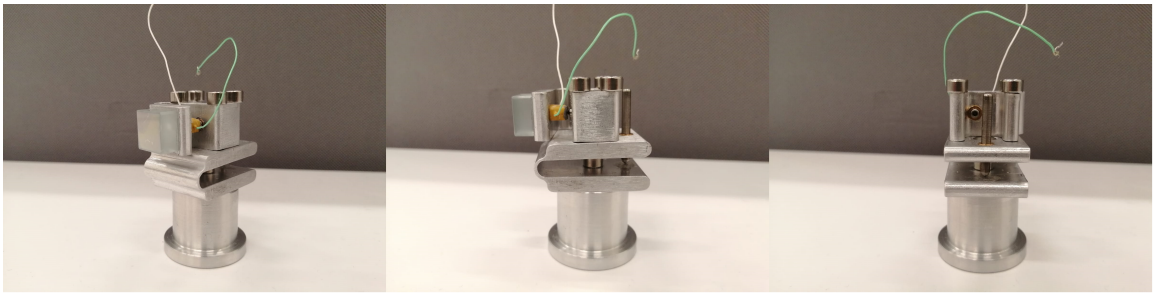

Figure 7: Images of the precision optical mounts designed and CNC machined to provide mechanical stability. The diffraction grating is attached to the left side of the upper part in the middle photo. Piezoelectric actuator is the yellow device seen in the middle and right photographs.

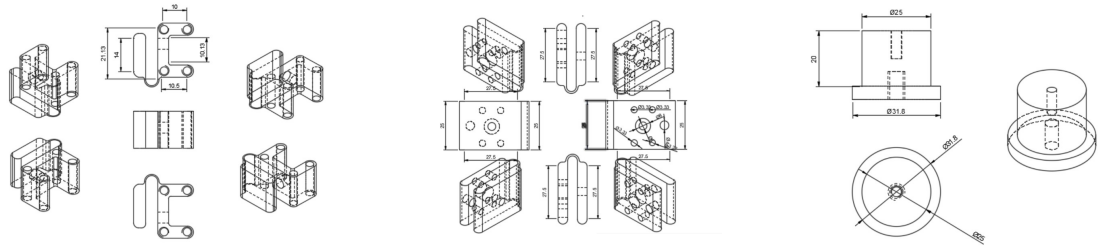

Figure 8: Drawings of the precision optical mounts which are designed to have the compact ECDL setup. This piece is needed to mount grating and the PZT which is used to change the angle of the grating. The mechanical part in the left drawing control the optical product in the pitch angle, while the mechanical part in the middle is used to control the optical product in the yaw angle. The mechanical part in the rightmost drawing is used for fixing these products stably.

is thought that it is necessary to cut the airflow in the laser system to increase the sensitivity, and the laser assembly is surrounded by a suitable metal aluminum box. The airflow changes the optical length of the outer cavity and causes a frequency shift of several hundred MHz in the long run.

In addition to mechanical disturbances, the problems created by thermal disturbances are an obstacle to obtaining a noise-free signal. An uneven temperature change of 1 °C creates a frequency change of approximately 2 GHz, and each nm change in outer cavity length creates a frequency change of 25 MHz [44]. The thermal linear expansion equation of the materials is given as follows.

$$\frac{L}{\Delta L} = \alpha T \tag{8}$$

Here, α is the linear expansion coefficient specific to each material, L is the length of the material, and ΔL is the length change due to temperature change. Considering that most of the products in the laser box are aluminum and we take the α value of about 23×10^{-6} °C^{-1} for aluminum, a temperature change of 0.1 °C causes a length change of approximately 2.3 nm in a 1 cm aluminum bar. This length variation causes significant uncertainty in the frequency of the laser. It has been observed that a person's standing close to (in cm level) or far from (m level) the laser assembly causes a temperature change of approximately 0.2 °C due to body temperature, and it has been realized that the thermal and mechanical stabilization of the narrow band laser assembly is inevitable. Because 0.2 °C temperature change causes a change of approximately 400 MHz in the frequency of the laser in our setup. Considering that the atomic transitions are 6 MHz, it is concluded that the temperature stabilization should be at the level of 10 mK [44]. However, since we provide frequency stabilization by applying a voltage to the piezo, which enables us to control the angle of the diffraction grating in ECDL, laser frequency changes due to temperature changes are compensated significantly. Since laser frequency depends on many different parameters such as the amount of noise of the laser diode current driver, the temperature of the

laser box, and the mechanical vibrations to which the assembly is exposed, the control effort with piezo alone may be insufficient. For this reason, it is necessary to minimize the fluctuations of each parameter or to perform active stabilization.

For the mechanical parts that move in yaw and pitch axes, the stress is distributed uniformly to the arc of the aluminum product. This means, the piece is reliable and does not have any single yielding point. Therefore, without going to the plastic region, those mechanical parts extends as they are designed. With the design, a simple and compact ECDL setup can be constructed and used easily. Using the ECDL configuration, one can build a low linewidth compact laser setup. Linewidth can be as low as kHz level, which is remarkably sufficient for atomic physics and spectroscopic applications [45].

3.1.2 Temperature controller

A PID controller is required for this type of precise temperature control for the laser box. For this issue, a standard industrial PID temperature controller, which is already present in the laboratory, is modified and used. With a Peltier device and a 20-k ohm thermistor, the mentioned temperature controller become suitable for an external temperature control process. Afterward, the PID parameters of the controller are adjusted specifically for the application, and it is seen that the error signal stabilizes after a few oscillations. NTC thermistors have a negative temperature coefficient, and their resistance decreases as the temperature increases. Measuring the resistance of these thermistors allows us to have direct information about the temperature. The equation describing the relationship between temperature and resistance of NTC sensors can be seen below.

$$R(T) = R_0 e^{B(\frac{1}{T} - \frac{1}{T_0})} \tag{9}$$

Here, the R_0 value indicates the resistance at T_0 temperature, and the B-coefficient is specific to each thermistor and is given as 4250 K in the aforementioned application.

Leaving the temperature alone in this equation, it can be written as,

$$T(R) = \frac{BT}{T_0 ln\frac{R}{R_0} + B} \tag{10}$$

After the temperature stabilization is achieved, all the instabilities in the device are removed and the device is made to work efficiently. Additionally, it is understood that it is important to fine-tune the current used by the laser diode. It has been observed that a current change of 1 μA causes an average frequency shift of 3 MHz, and this value is consistent with what is seen in the literature [44].

After the laser assembly is isolated and the mechanical and thermal stabilities are improved, rubidium atomic transitions could be followed with the oscilloscope in a constant and sensitive manner, and fluorescence is obtained for more than thirty minutes with passive laser stability.

3.1.3 ECDL efficiency

The power delivered by the ECDL setup used in this study is comparable to the other studies in the literature [42]. Power delivered to the different diffraction orders changes by the polarization of the light. Since the relative direction of grating rulings and polarization of the light is important, polarization is the main parameter that affects the ECDL efficiency. In this study, maximally 18 mW power is delivered to the output beam. Although 18 mW power is a modest value, it is enough to carry out laser cooling and spectroscopy experiments, since 5 mW power can be sufficient for atomic physics applications [35]. The reason for the low output power might be the grating ghosts since the blazed grating is used instead of the holographic one in this work. For example in Ref. [42], the holographic grating is used to avoid grating ghosts, which are unwanted maxima caused by the deviations of the distance between adjacent grooves as a consequence of inaccuracies during the ruling process. Another reason for the low output power might be the result of the choice of the grating. If a

grating that reflects a larger fraction of light back into the laser is chosen, that results in a broader discontinuous tuning range at the expense of reduced output power [42]. Even though the ECDL setup suggested in this study requires optimization, it offers a simple and compact solution for general usage.

Characterization of the ECDL can be further completed by measuring the linewidth which will be done using the self-heterodyne measurement [46]. Linewidth, which is expected to be on the order of the kHz level, could not be measured yet, however, it can be completed easily. Also, to further characterize the ECDL, a tuning range should be specified. Although the expected FSR is on the order of several GHz, with additional modulation techniques, it is possible to have an FSR on the order of a hundred GHz [47]. To conclude, it can be said that the Littrow configuration offers a good and simple configuration to obtain an ECDL to overcome the drawbacks of the free-running laser diodes such as the high linewidth and inability to tune. With a setup similar to the one offered here, one can cheaply construct a simple and compact ECDL that is ready to be used in the laboratory environment easily. With this setup, laser cooling and spectroscopy experiments become accessible and reliable even for educational purposes.

3.2 Frequency modulation (FM) spectroscopy

3.2.1 Frequency stabilization

Free-running laser diodes have a bandwidth of THz (nanometer in wavelength) and are not suitable for wavelength and frequency tunability. With the help of the ECDL method, it becomes possible to develop narrow linewidth lasers. However, precise frequency adjustability is needed for the laser to be in the exact desired atomic transition. By changing the angle of the diffraction grating, the frequency of the ECDL is controlled. For the most efficient MOT, lasers should be red-shifted 3-4 Γs from the desired atomic transition and should be prepared precisely. To lock the frequency of

the laser to the desired value, there are two conventional options in the literature. One is to lock the frequency of the laser to the central frequency of the optical cavity, and the other is to lock the frequency of the laser to the atomic transitions. Since the lasers are prepared to be used to manipulate the single ^{87}Rb atoms, locking to the atomic transition is more appropriate for our application. In the literature, one can find two similar setup configurations, which are called frequency modulation (FM) spectroscopy and modulation transfer (MT) spectroscopy [48, 49, 50, 51, 52, 53]. Even if both setups are extremely similar to each other, frequency modulation spectroscopy (FM Spectroscopy) technique, which is introduced in 1983 by Bjorklund and Levenson [51], gained more popularity over time. The MT Spectroscopy technique is introduced very close to the previous technique but is ignored for a long time [50]. The MT Spectroscopy technique has a significant advantage compared to the FM Spectroscopy technique and can be prepared with very similar experimental setups. The residual amplitude modulation (RAM) in the MT Spectroscopy technique is at very low levels compared to FM Spectroscopy [48]. The residual amplitude modulation is the unwanted non-zero amplitude modulation that is imprinted on the laser beam during the phase modulation process [54]. By minimizing the RAM, signals can be distinguished and resolved more precisely. Fig. 9 and Fig. 10 show schematics of FM Spectroscopy and MT Spectroscopy setups.

In these techniques, the frequency modulation of the laser is done with the help of the electro-optical modulator (EOM), which consists of Pockels cells whose refractive index varies linearly with the applied electric field. Taking advantage of this effect, electro-optical modulators can be used as phase modulators. In the above arrangement, the laser beam is sent directly to the electro-optical modulator. After passing through the electro-optical modulator, two sideband signals are formed in addition to the carrier signal.

Let's say the incoming signal has frequency ω and can be described as follows,

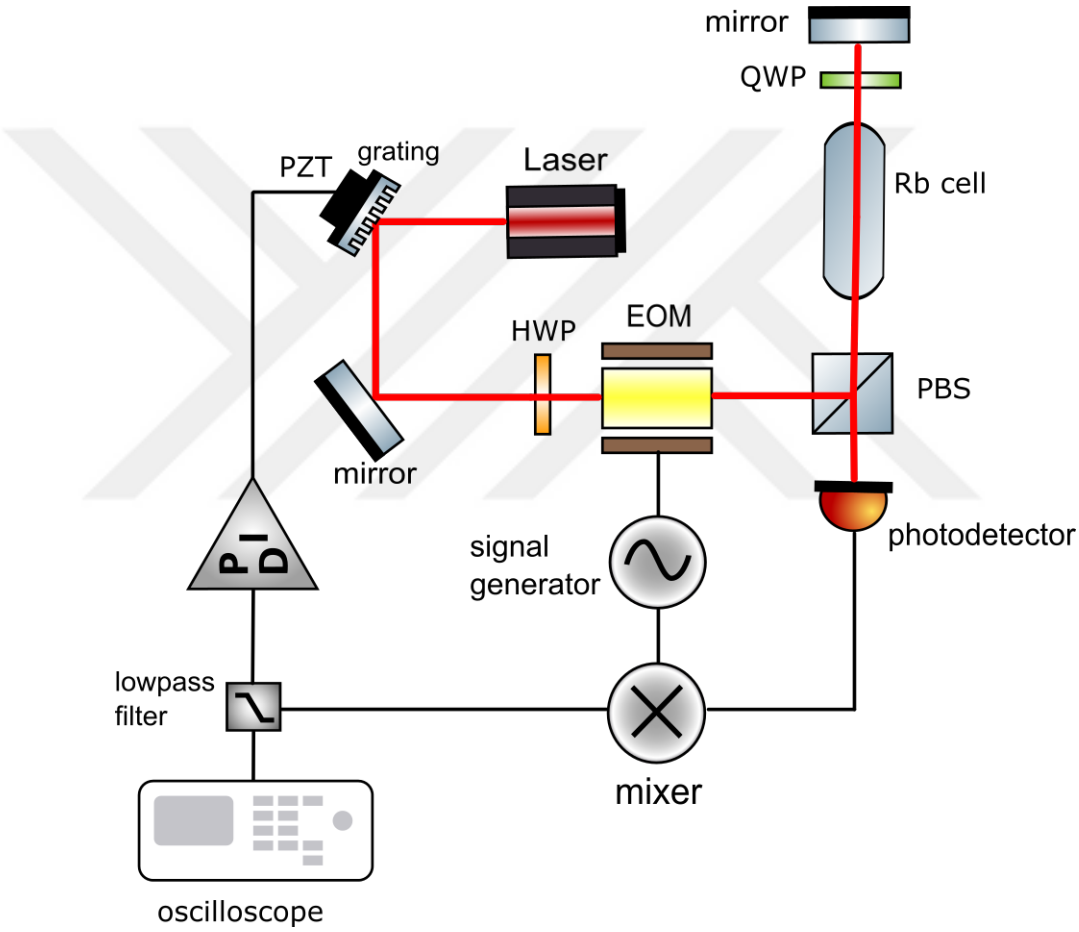

Figure 9: Schematic representation of the FM spectroscopy setup used for tracking atomic transitions and laser frequency locking.

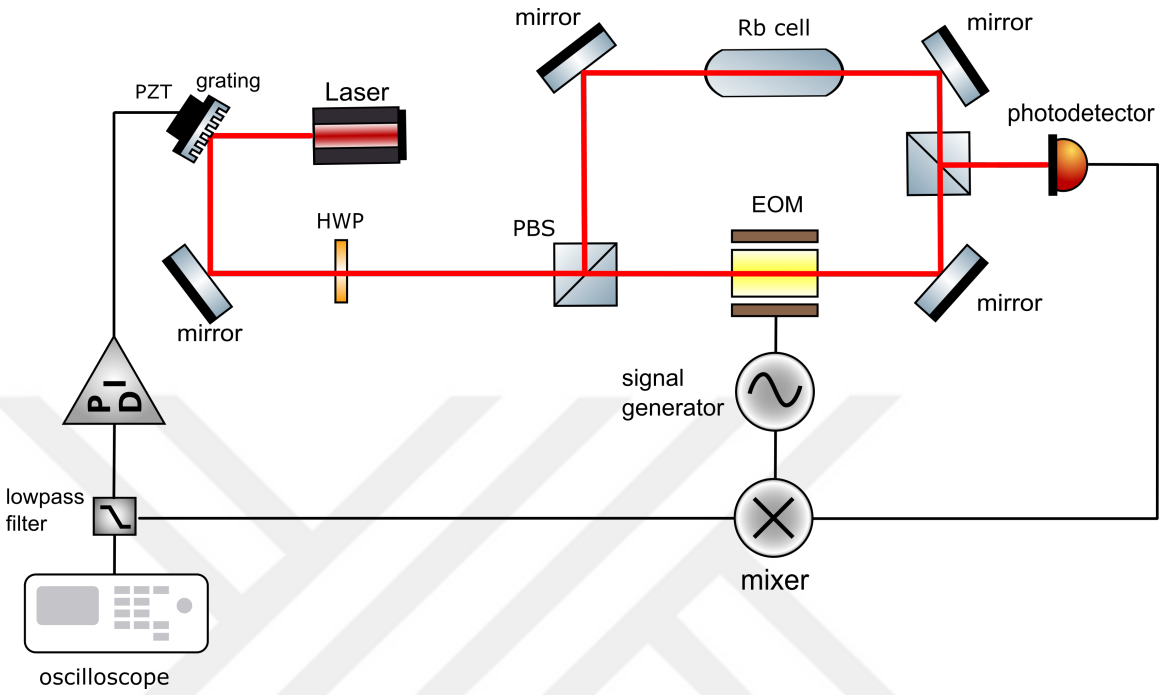

Figure 10: Schematic representation of the MT spectroscopy setup given as a reference and comparison with the FM spectroscopy setup.

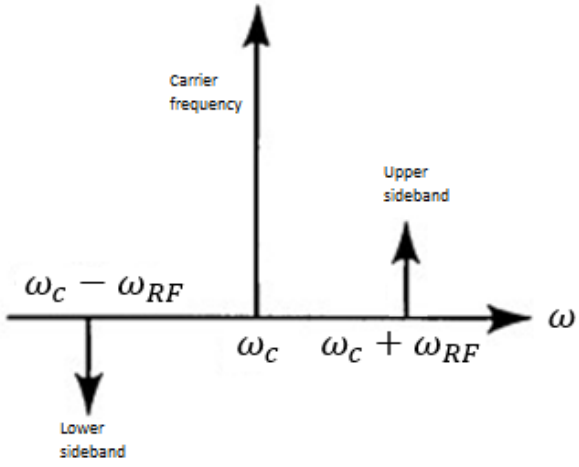

Figure 11: Carrier and sideband signals shown in the frequency domain.

$$S = Ae^{i\omega t} \tag{11}$$

where A is the amplitude of the incoming signal. If the sinusoidal voltage difference is applied to the EOM with amplitude β and the frequency ω_{RF}, the above signal becomes,

$$S = Ae^{i\omega t + i\beta sin(\omega_{RF} t)} \tag{12}$$

If the β is small, the above equation can be Taylor expanded and return as,

$$S = Ae^{i\omega t}\Big(1 + i\beta sin(\omega_{RF} t)\Big) \tag{13}$$

and writing the sine function in terms of exponential gives,

$$S = Ae^{i\omega t}\Big(1 + \frac{\beta}{2}(e^{i\omega_{RF} t} - e^{-i\omega_{RF} t})\Big) = A\Big(e^{i\omega t} + \frac{\beta}{2}e^{i(\omega+\omega_{RF})t} - \frac{\beta}{2}e^{i(\omega-\omega_{RF})t}\Big). \tag{14}$$

The right-hand side of the equation above, clearly shows that the carrier signal has two sidebands after passing through the electro-optic modulator. One sideband is described by the frequency of $\omega + \omega_{RF}$ and the other one is described by the frequency of $\omega - \omega_{RF}$. Carrier and sideband signals are shown in Fig. 11.

These sideband signals are located symmetrically to the carrier signal. It can work like pump-probe spectroscopy by adjusting the polarization of the modulated signal sent to the atomic gas cell. Having two mutually transmitted signals is critical to avoiding the Doppler effect due to atomic motions and to observing precise atomic transitions. Polarization of the output beam of the ECDL is controlled by the half-wave plate to make it work efficiently with the EOM. After being modulated by the EOM, the beam is sent through the reference cell which is called a pump beam. The pump beam saturates the atomic transitions and excites half of the ^{87}Rb population. After the reference cell, the polarization of the beam is changed by 90° with the help of

the quarter-wave plate and the mirror. This beam is called a probe beam and as the name implies helps us to ”probe” the hyperfine transitions together with the pump beam. Absorption due to a single beam can be seen as a dip in the atomic absorption spectrum. If two mutually orthogonal beams are used, due to the stimulated emission and ability to address the same slow-moving group of atoms, hyperfine transitions can be traced. By addressing the slowly moving same group of atoms, the Doppler broadening effect can be avoided. Due to the pump-probe spectroscopy, additional transition peaks also appear in the absorption spectrum which cannot be seen by the single beam. These transitions occur exactly halfway between two ”physical” transitions. When the frequency is scanned through a range, right in the middle of two transitions, due to their velocity, atoms might be red-shifted to a lower transition while blue-shifted to an upper transition, resulting in the increased intensity of the probe beam. These extra transitions seen in the absorption spectrum are called crossover transitions and might be stronger than the actual physical transitions. Pump-probe spectroscopy is also called saturated absorption spectroscopy [55, 56, 41]. For detailed information about laser spectroscopy see Ref. [27, 28]. Atomic transitions obtained with the help of saturated absorption spectroscopy are measured with the help of a photodetector and then detected by a standard RF frequency detection method with the help of an RF mixer. Carrier and sideband signals are sent to the atomic gas cell and then to the RF mixer. The carrier signal creates a beat note with each sideband signal. If the carrier signal exactly corresponds to the desired atomic transition, the beat note created by the carrier with each sideband cancels each other and does not output any error signal. If the frequency of the carrier signal is shifted to the right or left relative to the atomic transition frequency, the beat note does not cancel each other out and outputs a positive or negative DC signal depending on the direction in which the signal is shifted. By looking at the output, it is possible to control the frequency of the laser with the PID controller and lock it to a certain atomic transition.

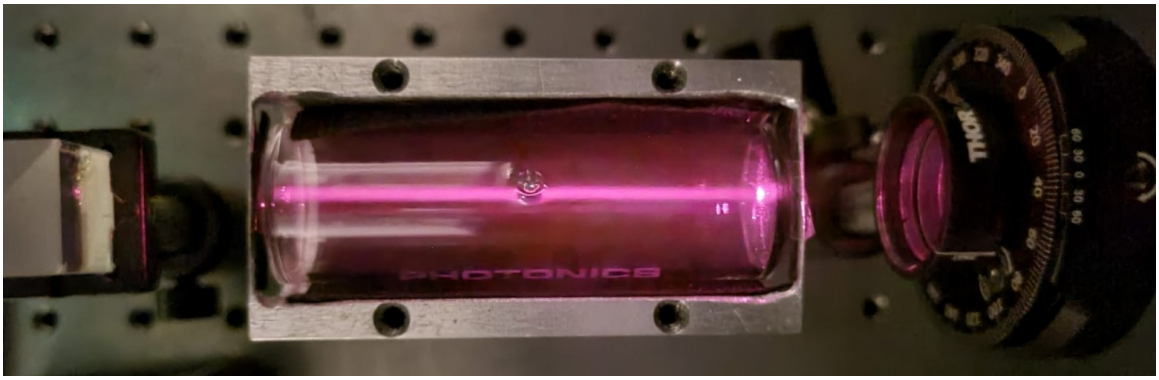

Figure 12: ^{87}Rb fluorescence image. When the laser frequency coincides with the ^{87}Rb D_2 line transition, the bright fluorescence is seen as shown in the figure.

A photo of the simple FM Spectroscopy setup can be seen in Fig. 13. As a result of the work described here, an error signal is obtained but noise reduction work should be done further. For frequency locking, an open-source proportional-integral-derivative controller (P-I-D) code, written by other researchers, is being used. These codes have been adapted to our application, and necessary tests have been made.

3.2.2 Rb transitions

The developed lasers are examined in the ^{87}Rb atomic gas cell and the corresponding rubidium fluorescence can be seen in Fig. 12. The linewidth of the laser has been successfully narrowed and ^{87}Rb atom transitions can be successfully scanned. An exact linewidth can be measured by further work. The probe beam is traced from the oscilloscope to see the relevant rubidium transitions and monitor the saturated absorption spectroscopy output. The oscilloscope trace and graph can be seen in Fig. 14 and Fig. 15.

The atomic transitions seen on the oscilloscope trace in Fig. 14 and Fig. 15 correspond to the D_2 transition of the ^{87}Rb atom and are used to obtain the error signal. In Fig. 16 we see the atomic transitions of both isotopes of the rubidium atom. These isotopes are found in nature as ^{85}Rb and ^{87}Rb, with a percentage of 72.17% and 27.83%, respectively. The reason why we see the transitions of both rubidium

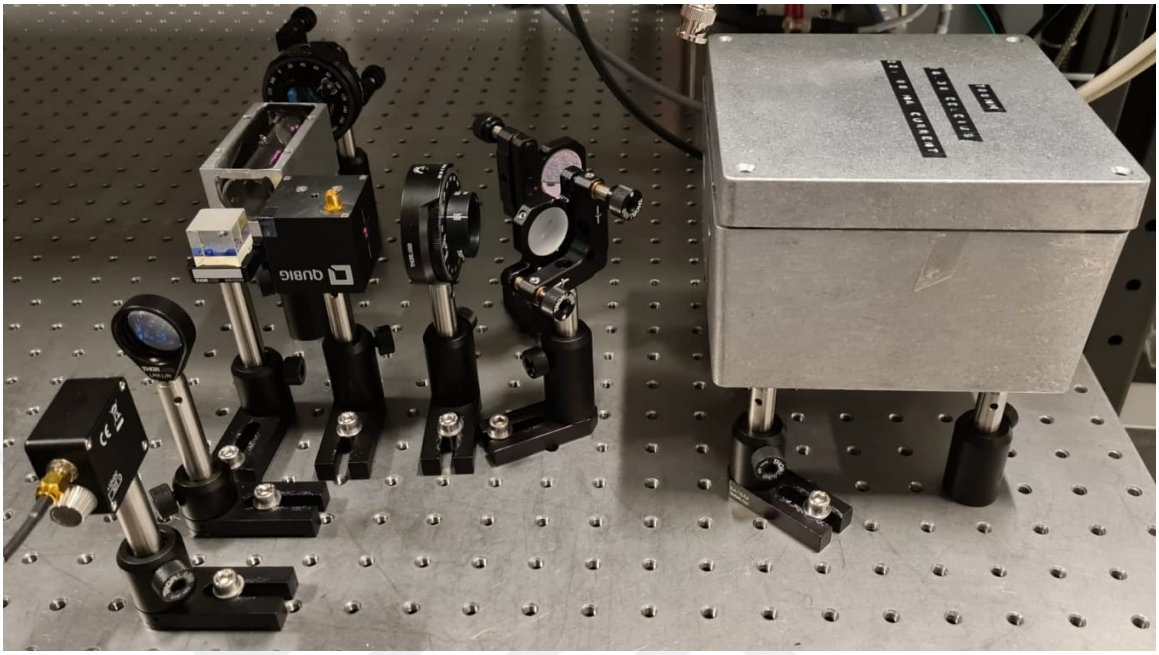

Figure 13: FM spectroscopy setup which is used for tracking atomic transitions and laser frequency locking.

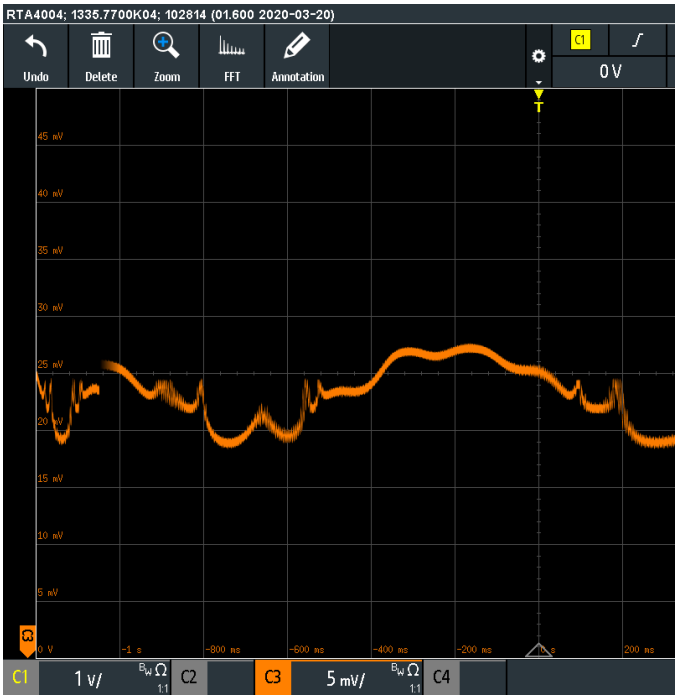

Figure 14: Oscilloscope image of rubidium atomic transitions obtained when scanning with piezoelectric actuator. The atomic transitions shown in the figure correspond to F=2→F' transitions and are located in the D_2 line of the ^{87}Rb atom.

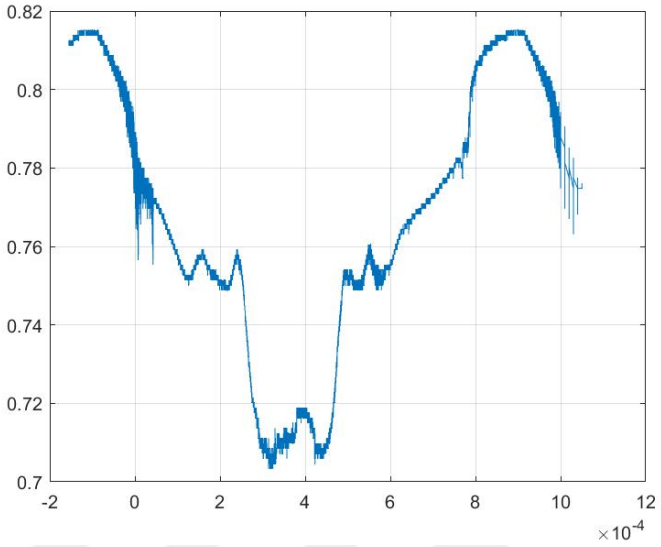

Figure 15: Plotted oscilloscope trace of rubidium atomic transitions obtained when scanning with piezoelectric actuator. The atomic transitions shown in the figure correspond to F=2→F' transitions and are located in the D_2 line of the ^{87}Rb atom.

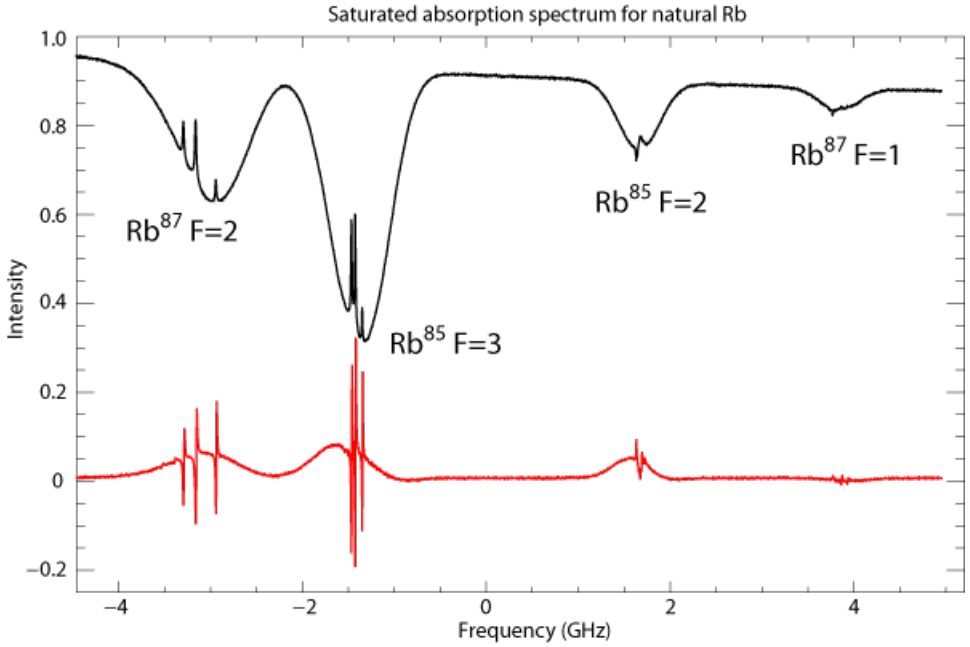

Figure 16: ^{87}Rb and ^{85}Rb atomic transitions and the corresponding error signals shown together [2].

isotopes in Fig. 16 is that the rubidium cell used in the aforementioned study contains both isotopes. Since only ^{87}Rb isotope will be used in our studies, the Rb gas cell purchased contains only ^{87}Rb isotope, and the atomic transitions mentioned in Fig. 14 and Fig. 15 correspond to the transitions on the far right and left in Fig. 16. From Fig. 15, D_2 line transitions of ^{87}Rb isotope can be easily recognized. From left to right, those little bumps correspond to F=2 $\rightarrow$ F'=CO13, F=2 $\rightarrow$ F'=CO23, and F=2 $\rightarrow$ F'=3 transitions.

3.2.3 Cooling and repump beams

The atomic transition to be used for cooling is the F=2 $\rightarrow$ F'=3 transition in the D_2 line of the ^{87}Rb atom. This atomic transition is preferred because it has easy access and because of the selection rules, it is less likely to decay to the dark state. The locking transition we use to adjust the frequency of the laser to the cooling transition is again the F=1 $\rightarrow$ F'=1 line of the D_2 transition of the ^{87}Rb atom. The laser locked in this line is used for cooling by shifting the frequency of approximately 400 MHz (200 MHz x 2) with a double-pass from the AOM. A repump laser is used to have access to the atoms that decay to the dark state and make the re-enter the cooling cycle. This laser is on the D_1 line and targets the transition of F=1 $\rightarrow$ F'=2 [57]. In order to target this transition, the frequency of the laser is locked to the F=1 $\rightarrow$ F'=CO12 transition on the same line, and it is produced by shifting 400 MHz with the help of AOM. For the probe laser, the F=2 $\rightarrow$ F'=3 transition of the D_2 line is used again, and locking lasers of the same configuration can be used for this transition [57]. In the light of the above information, a collective assembly including whole locking, cooling, and repump lasers can be seen in Fig. 17. D_2 line hyperfine levels of ^{87}Rb can be found in Fig. 44.

Acousto-optic modulators (AOM) are optical modulators that are used in switching, signal modulation, or frequency control. They harness the acousto-optic effect to

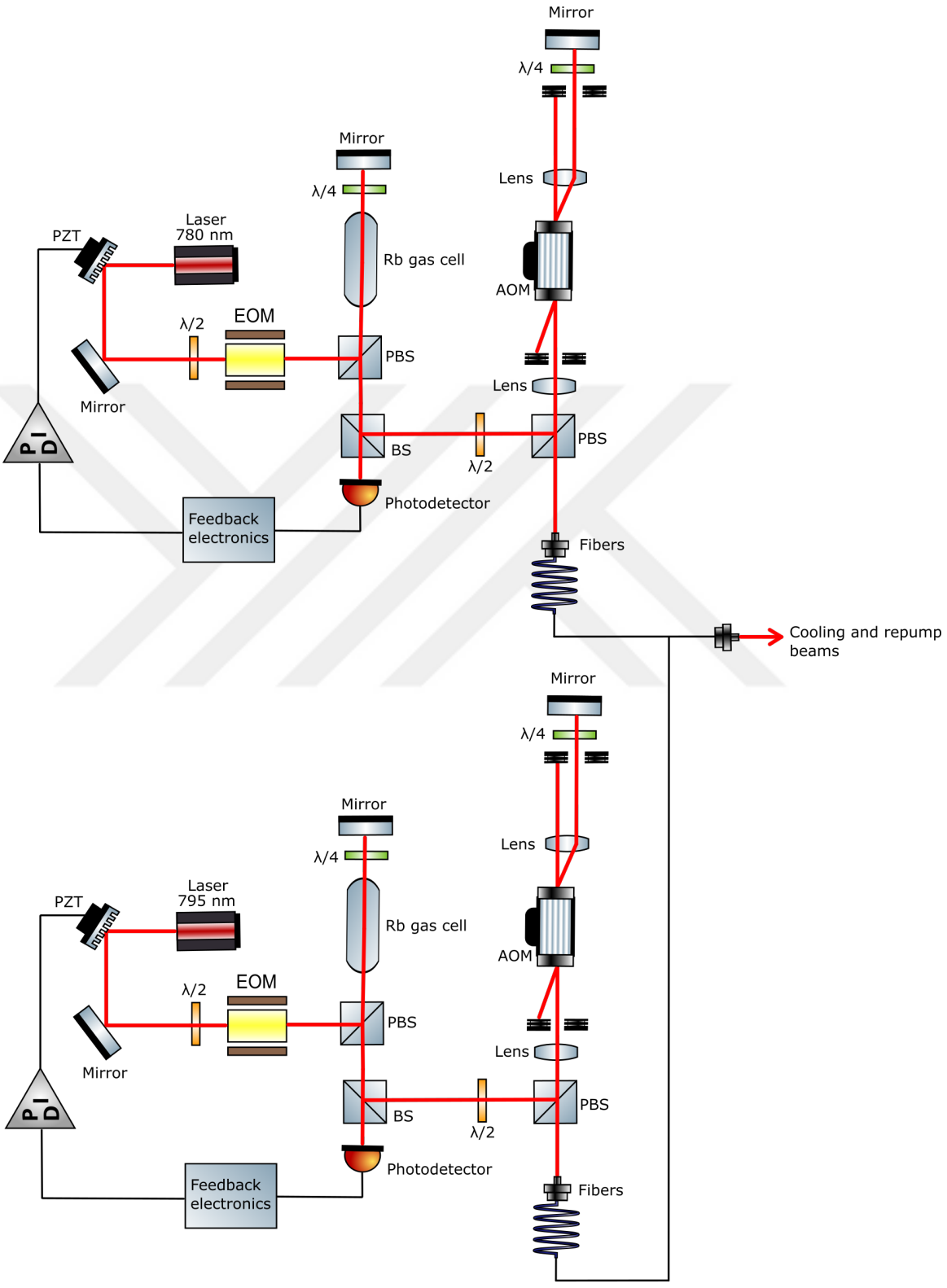

Figure 17: Total MOT setup showing the preparation of cooling and repump beams together with their locking setups. 200 MHz AOM's are used to compansate the frequency difference between locking-cooling and locking-repump beams.

diffract and shift the light frequency using the sound waves as its name implies. An RF signal is applied to the crystal creating a change in the refractive index. Because of their working principle, they are also called Bragg deflectors. AOMs used in this work shift the frequency of the light for a specific value to match the frequency difference of the locking and cooling transitions. The same applies to locking and repump transitions also. When the light passes the AOM, higher-order beams can be easily noticed depending on the alignment of the device. By changing the relative position of the beam and the device, -1, +1, or 0th orders can be maximized. By looking at the shape of the 0th order beam, AOM alignment can be understood. 0th order beam has to have two distinct, smaller, spatially distinguishable beams and their relative positions should be symmetrical. Using the 200 MHz frequency shift with the AOM in double-pass configuration, 400 MHz frequency compensation can be achieved.

CHAPTER IV

ULTRA-HIGH VACUUM SETUP AND RB SOURCE

4.1 General vacuum setup

When trapping atoms with the magneto-optical trap method, we need to ensure that the atoms stay in the trap as long as possible. As can be noticed, this is impossible at atmospheric pressure because the molecules in the air make it impossible for us to reach the rubidium atoms or prevent any atoms from being trapped by molecular collisions. Therefore, minimizing molecular collisions is a must to increase MOT efficiency. To do this, an ultra-high vacuum setup must be installed. The ultra-high vacuum setup roughly corresponds to pressure levels lower than the picobar levels, and the lower this level the higher the success of the MOT setup will be. Generally, the prevailing regime at atmospheric pressure and near pressure levels is described by molecular collisions, but at ultra-high vacuum levels molecular collisions are now virtually zero, and an atom is less likely to collide with the walls of a pump or vacuum chamber than with another atom. From these pressure levels, the mean free path of an atom rises to 40 km. In order to reach the ultra-high vacuum level, our vacuum chamber needs to be pumped down with the help of different pumps. The vacuum regime between 1 mbar and 10^{-3} mbar is called an average vacuum, the section from 10^{-3} mbar to 10^{-7} mbar is called high vacuum and pressure levels lower than 10^{-7} mbar are called ultra-high vacuum. In order to reach the desired pressure level, we need to use roughly 3 different pumps. Although it is necessary to use different pumps for each vacuum level, it is also important in terms of guaranteeing a long pump life. Turbo pumps are one of the standard solutions used to reach high and ultra-high vacuum levels. The blades, which are in a row inside, are the main element that

determines the working principle of this pump.

These blades rotate and push the molecules mechanically in the vacuum chamber and throw them out of the exhaust section. However, after reaching a certain pressure level, the turbo pump will be insufficient to pump down further, because of the high pressure in the exhaust. As can be understood, working against atmospheric pressure in the exhaust section will force the turbo pump too much and lower its efficiency. For this reason, a second pump is needed to assist the turbo pump. This second pump needs to create a rough vacuum in the exhaust section for the turbo pump to work properly. Although this vacuum is not as low as the vacuum obtained with the turbo pump, it is sufficient to be at mbar levels. This second pump is called a "backing pump" because of its auxiliary function. In addition, this pump can be used to reduce the pressure of the vacuum chamber before the turbo pump to make the operation of the turbo pump efficient. After obtaining a high vacuum with the help of these two pumps, an additional pump is needed for ultra-high vacuum levels and for cleaner operations which is the ion pump. The working principle of ion pumps is simple but very efficient. These pumps ionize the gases inside the chamber and apply a high electrical field and capture the ionized atoms by sending them to the electrode. Thus, it is possible to capture these particles even at very low-pressure values. We can simply classify ion pumps into three groups. These are CV/diode pumps, DI/ noble gas diode, and triode pumps.

The diode pump provides the highest pumping speed, vacuum quality, and electrical stability for reactive gases, but is not suitable for long-term inert gas pumping. DI pumps, on the other hand, are more successful in pumping long-term noble gases, although they do not have a speed as high as CV pumps. Triode pumps are a mix of these two. The use of a diode pump will be more appropriate within the scope of this project. It is always possible to use the titanium sublimation cartridge in addition to the ion pump if the sufficient pressure value cannot be reached. With the use of the

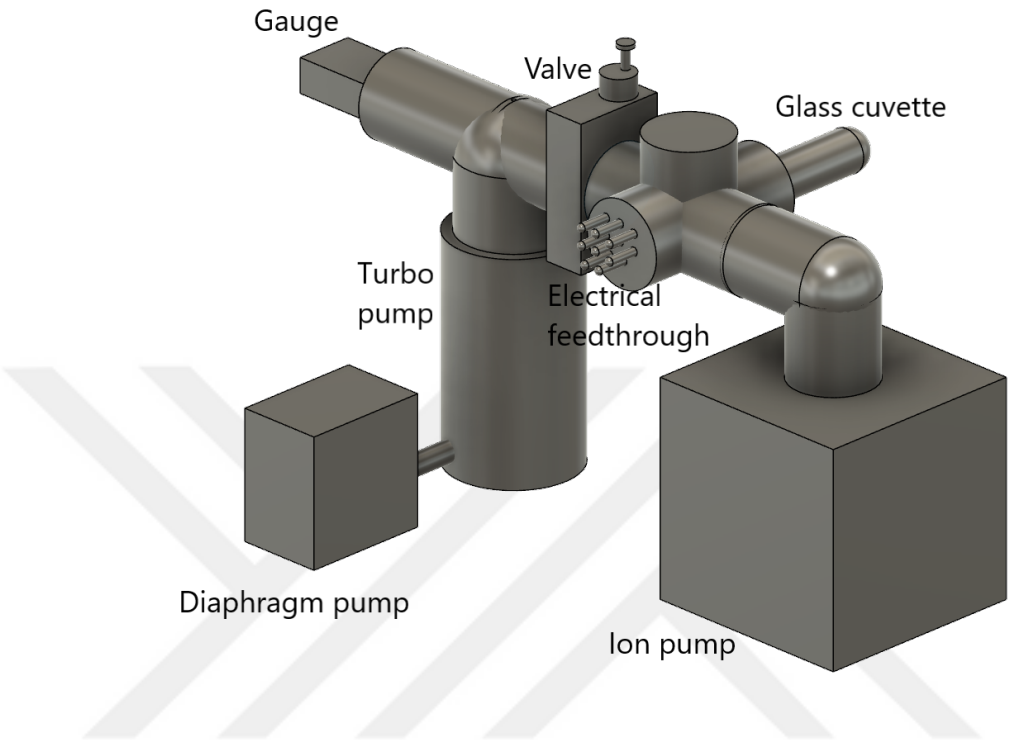

Figure 18: 3D vacuum drawing of the complete setup. Rough and high vacuum pressure values are measured by the gauge on the left, whereas the ultra-high vacuum pressure measurement is done with the integral gauge of the ion pump.

ion pump, it is now possible to go down to 10^{-11} mbar levels. You can see the simple diagram of the mentioned vacuum setup in Fig. 18 and Fig. 19. As can be seen in Fig. 18 and Fig. 19, the turbo pump and backing pump are connected to the vacuum chamber together and work harmoniously. After reaching the desired pressure level, the turbo and backing pump must be disconnected from the vacuum chamber with the help of an ultra-high vacuum valve. After a certain vacuum level, the ion pump is turned on and the valve which separates the turbo and ion pump is closed. After that stage ultra-high vacuum is provided by the ion pump only.

It is also possible to measure pressure with an ion pump with the help of additional accessories because as it is known, ion pumps ionize the gases inside and capture

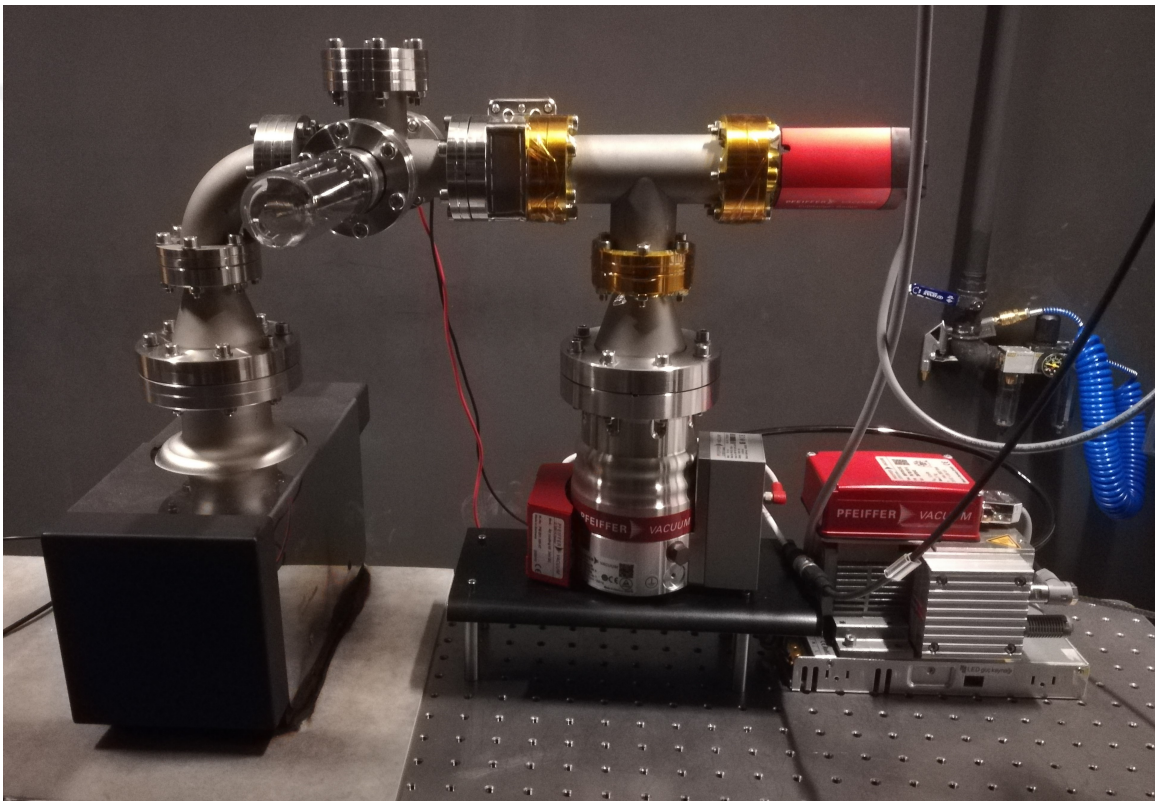

Figure 19: Image of the complete UHV setup given from the different angle. Due to the vibrating nature of the diaphragm pump, it is place outside the optics table unlike the image shown here.

them with the help of an electric field. These captured ions create a current and if necessary, calibration is done, and it is possible to use this current value to measure the pressure inside [58]. After creating our system, it is the most important practice to clean the system and remove possible contaminants before starting any vacuuming process [59]. All system components should be washed first with a mild detergent. Then, the components should be cleaned again with demineralized water to get rid of detergent residues. All cleaning with an ultrasonic bath should be repeated to make sure we get rid of any detergent residue. Then, the system should be cleaned again with analytical grade acetone and analytical grade ethanol, respectively. Finally, it is dried with pressurized nitrogen and the cleaning process is completed. Finally, the residues in the system are tried to be removed from the system with the help of heat. During this process, the whole system is wrapped with aluminum foil and heated to high temperatures. This process is called baking and for details see Ref. [60].

4.2 Vacuum without the ion pump

The minimum vacuum values required for the magneto-optical trap are in the range of 10^{-9}-10^{-10} mbar. These values are obtained with the diaphragm pump and the turbo pump only, and the time-dependent pressure changes can be seen in Fig. 20 and Fig. 21. As can be seen in Fig. 21, the pressure value obtained after one day with only the diaphragm pump and turbo pump is at the level of 10^{-9} mbar. After exactly 28 hours and 15 minutes, a pressure level of approximately 7.4×10^{-9} mbar is reached. A pressure level of 10^{-9} mbar is sufficient for the magneto-optical trap and reaching these levels with only the backing pump and the turbo pump is the result of a very carefully prepared vacuum design. It is not usual to observe ultra-high vacuum with only turbopump in the literature and experiments can be done with turbopump without the need for ion pump support. However, the vibrational nature of the turbo pump, even if it is very small, is an obstacle for tasks that require precision such as

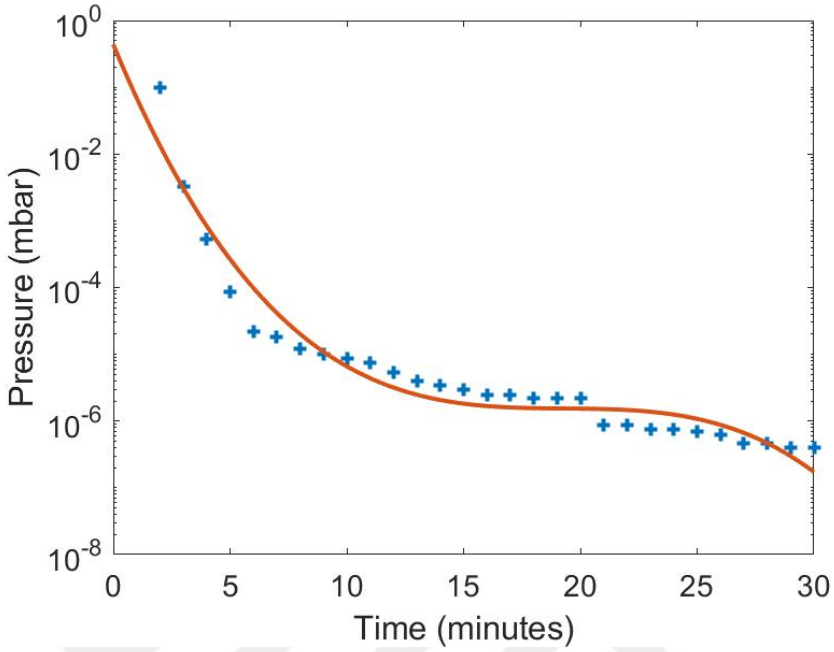

Figure 20: Pressure values obtained in the first 30 minutes with the diaphragm pump and turbo pump. The blue data points in the graph are time dependent pressure values, and the red curve is represented by a 3rd order polynomial function.

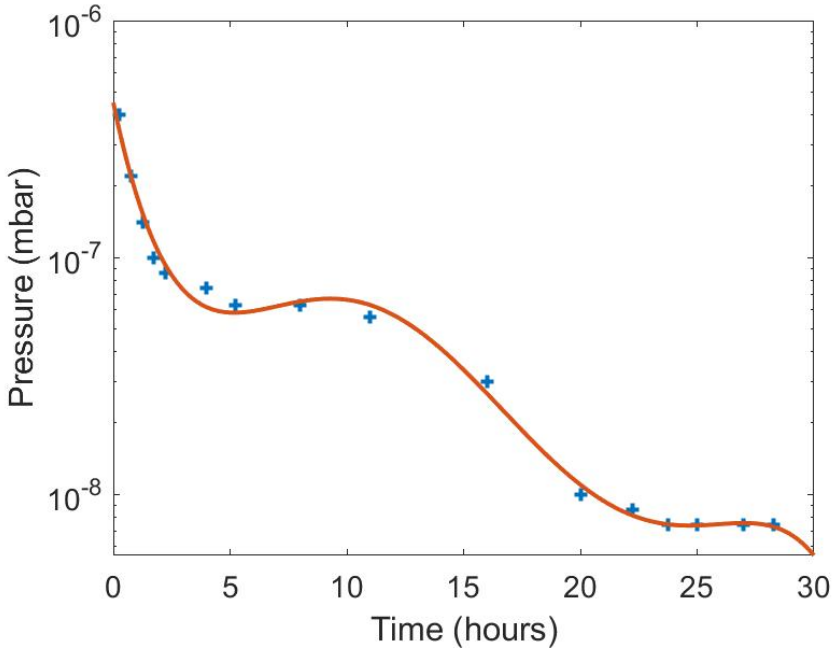

Figure 21: Pressure values obtained at the end of a day with diaphragm pump and turbo pump. The blue data points in the graph are time dependent pressure values, and the red curve is represented by the 5th order polynomial function.

single-atom trapping and stabilization of frequency-locked lasers. For this reason, an ion pump is installed in the setup, and it is decided that it would be more appropriate to start the optical processes with the turbo pump turned off and only when the ion pump is running. The ion pump is one of the most important parts of ultra-high vacuum experiments due to its quiet and clean operation. In addition, the use of an ion pump is essential to achieve pressure levels beyond 10^{-10} mbar.

4.3 Vacuum with the ion pump

As discussed above, to have a cleaner vacuum operation, the ion pump is needed and it is installed in the setup. From the first few trials, it is seen that the ion pump itself is outgassing and cannot help the turbo pump to pump down further. Theoretically, with the help of the additional pump, the vacuum level should be lower than the 10^{-9} mbar level. However, together minimum pressure value that can be reached is no lower than 10^{-9} mbar. Pump-down behavior of the whole system can be seen in Fig. 22 and it is understood that the system needs to be baked.

As can be seen in Fig. 22, the pressure of the turbo pump also increases as soon as the ion pump starts to work and after a while, the pressure values become equal. This makes us think that the ion pump outgasses and shows that we need to bake out the system to minimize this effect. This process is done in order to evaporate unwanted substances, especially water vapor, which is the most important pollutant of vacuum systems and throw them out of the system. While baking, the entire vacuum assembly should be heated to the same temperature, together with the heaters integrated into the pump. The ion pump integrated heaters heat up to 250 °C and the pump itself withstands a temperature of 350 °C. The turbo pump can withstand temperatures of 120 °C and 200 °C with the valve open and 150 °C closed. The limiting factor here is the turbo pump, and it is planned to heat the entire system up to 120 °C. In order for the pressure gauge to be heated during the bake-out, the electronic unit must be

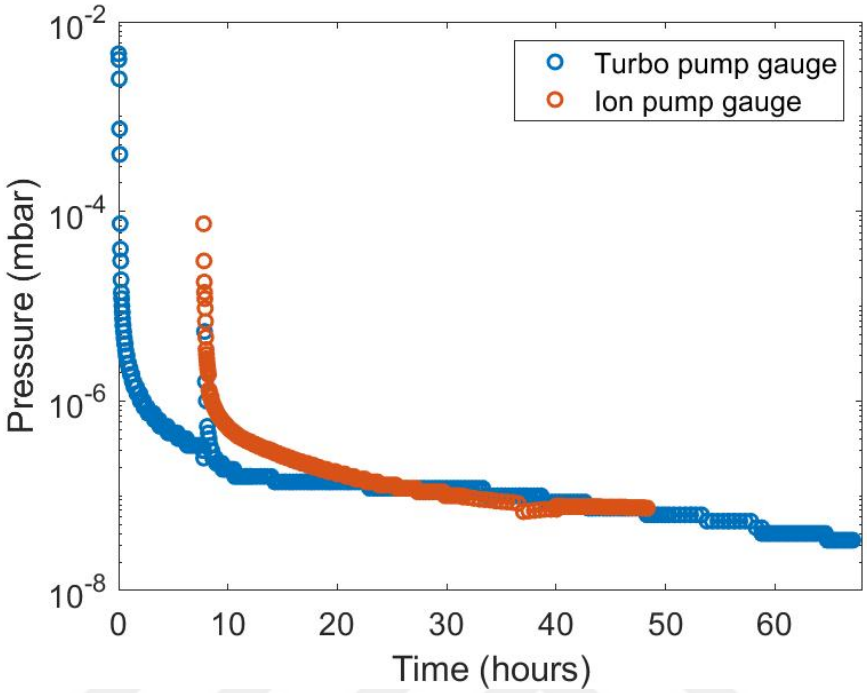

Figure 22: Ion and turbo pump pressure graph. From the figure, it is seen that the pressure values cannot reach $10^{-}9$ mbar level and baking is decided.

removed, and without the electronic unit, it can withstand a maximum temperature of 55 °C. For this reason, pressure measurement could be made only when the ion pump is on during the baking process.

4.4 Baking

For the process, firstly, the wires are selected so that they can deliver the desired heat through the system. The selected wires are 1500-watt standard oven wires and offer an inexpensive and simple solution for the baking process. The wires are first tightly wrapped on a rectangular piece of cardboard so as not to short-circuit which can be seen in Fig. 43, and then covered with a kapton tape which has high heat permeability but low electrical permeability. The purpose of this is to prevent the wires from short-circuiting when they are covered with aluminum foil to distribute the heat evenly through the whole system. Afterward, it is wrapped with several layers of aluminum foil and made ready for isotropic heat distribution. It is seen that reaching

75 °C in a short time with a current of 1 ampere is possible with this configuration. However, it has been observed that the desired temperature can be reached with a current of 6-7 A.

It is predicted that the tested wires could easily reach 120 ° with a higher current, and baking preparations are started. First of all, the ion pump's own heater, which can reach 250 °, is attached to its place on the pump and fixed with screws. Except for the turbo pump, the entire vacuum system is covered with 3 layers of aluminum foil. This is done both to avoid minute contact between the wires and the vacuum and to spread the heat evenly. The wires are then wrapped tightly around the system and covered with kapton tape to prevent electrical short circuits again. The preparation stage for baking can be seen in Fig. 23.

Finally, the entire system, except the turbopump, is covered with 3 layers of aluminum foil again, and it is aimed to keep the heat in the vacuum system. After the high current sources are supplied by combining four standard power supplies, the baking process is started. While the initially anticipated duration of the procedure is 48 hours, the application took approximately 60 hours. The final stage photograph of the prepared baking system is shown in Fig. 24.

It took about 8 hours to reach the targeted 120 °C after the heating process started. Heating and cooling processes must be done very slowly so that there is no leakage at the connection points and no cracking due to the different expansion coefficients in the glass-metal connection. One of the most important points in the baking process is that the heat is spread evenly throughout the system. When heat is not evenly distributed throughout the system, water vapor tends to condense in cooler regions. The turbo pump is an exception to this, as it is the main evacuation channel. Since the turbo pump is the coldest place in the system, the airflow inside the system will be towards the turbo pump, that is, out of the system.

Three thermocouples are installed in contact with the steel surfaces of the vacuum

Figure 23: Image of the intermediate stage assembly in the preparation of the baking apparatus. Complete setup is wrapped with wires, aluminum foils and kapton tapes.

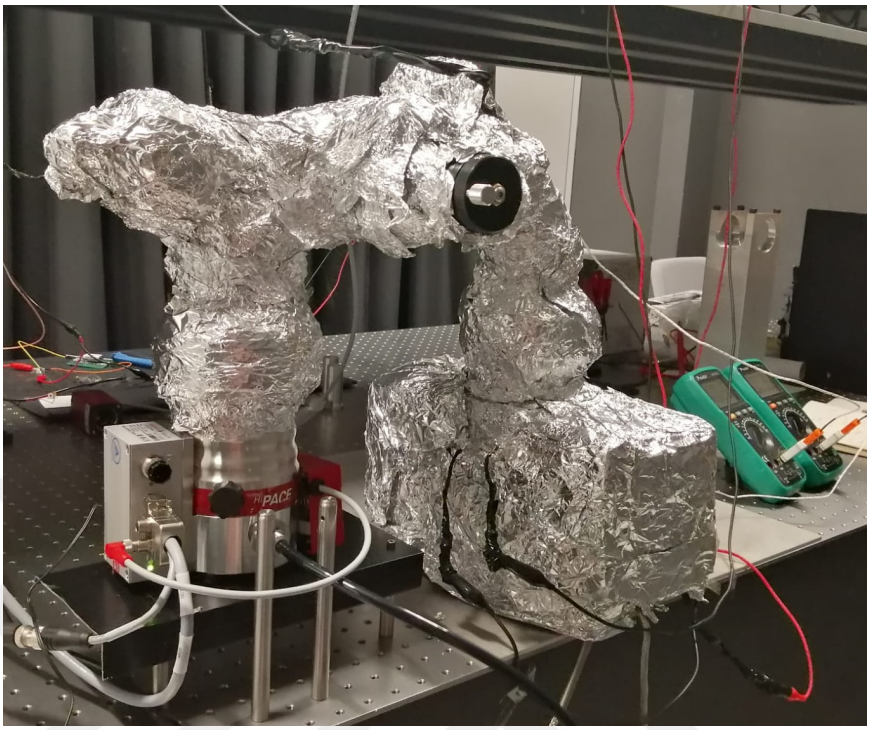

Figure 24: Image of the final stage assembly in the preparation of the baking apparatus. Complete setup is wrapped with wires, aluminum foils and kapton tapes.

system elements and these values are noted at certain time intervals. The highest value seen in the heat meter of the ion pump is recorded as 207 °C, the highest value observed in the glass-metal connection is 64 °C, and the highest value observed in the turbo pump connection is recorded as 41.9 °C. Although there is a very serious difference between the values, since the temperature gradient decreases towards the turbo pump, the water vapor did not condense and could be discharged from the system via the turbo pump.

During the baking process, first of all, the diaphragm pump and the turbo pump are operated as usual, and the turbine of the turbo pump is expected to reach the optimum rotation frequency (1500 Hz). After this stage, the heaters are operated in a controlled manner and the current level is increased gradually to increase the heat. After reaching 120 °C, it waits for 12 hours, and the ion pump is turned on. However, since the electronic unit of the vacuum gauge is removed, only pressure

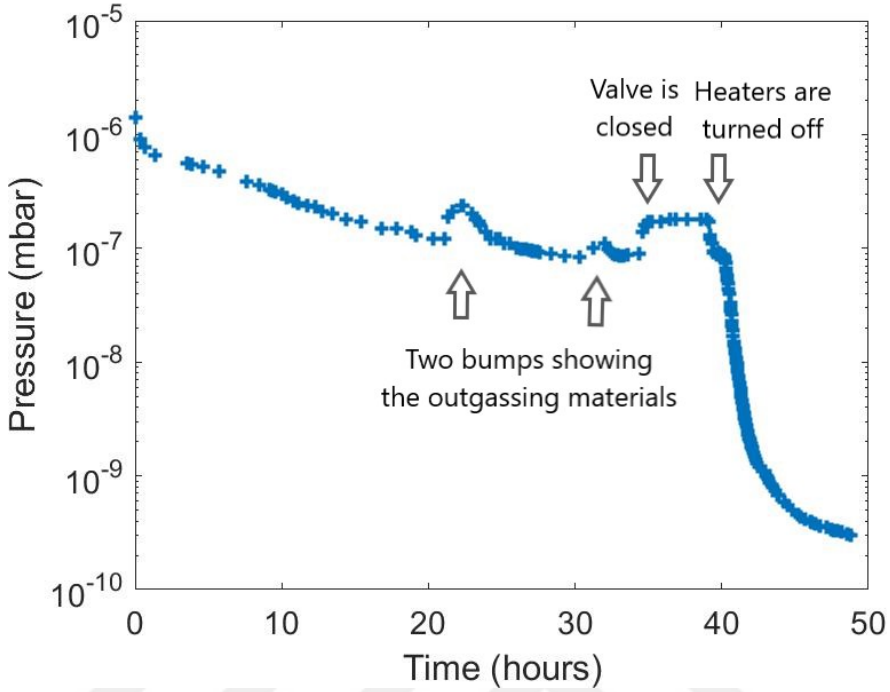

Figure 25: Pressure graph during the bake-out operation. Values obtained after the ion pump is started. Arrows describe the main changes during the bake-out process.

measurements are done after the ion pump is started. The very first value seen on the ion pump controller, which is 1.9×10^{-8} mbar, is noted. Then, it waits until the pressure value reaches saturation and the valve separating the turbo pump from the system is closed. Afterward, it is waited for another 6 hours and the heaters are turned off in a controlled manner. As a result of the process, a pressure value of 2.5×10^{-10} mbar is reached. The pressure values recorded during the baking process are shown in Fig. 25. If some contaminants start to decompose, the pressure of the whole system increases accordingly. Two small bumps are seen in Fig. 25, which demonstrates the presence of the outgassing organic material.

4.5 Rb Source

Dispensers that are used in this work are the alloys of the rubidium with bismuth metals. Rubidium, an alkali metal, forms a stable bond with bismuth, which has a high melting point. When rubidium, which has a lower melting point alone, alloys with

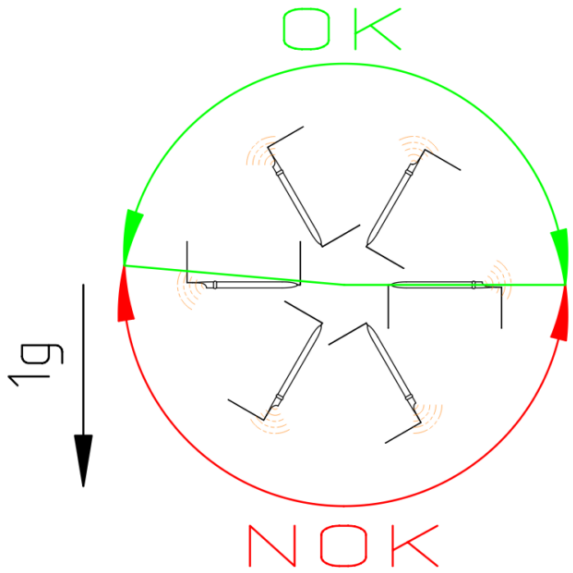

Figure 26: Combinations of connecting the rubidium dispensers to the vacuum electrical feedthrough. 'OK' means suitable and 'NOK' means not suitable. The exit direction of the rubidium atoms is shown in brown [3].

bismuth, its melting point increases and becomes suitable to be used as a source. A small stainless-steel tube is filled with this alloy and coated with indium. This coating melts during the baking process or when it is first powered with the heating current. The current flowing through the dispenser then releases the rubidium atoms in a single axis. Before baking, the rubidium dispensers are fixed to the electrical feedthrough and mounted to the vacuum setup in order not to be opened again so that the vacuum system is not exposed to the atmosphere. Aluminum cable lugs have been disinfected and used for this task, which needs to be worked very meticulously. Aluminum, which has a low outgassing rate, is used as a connecting element between the rubidium dispenser and the electrical feedthrough pins. The system that integrates the Rb dispenser into the vacuum system is shown in Fig. 27. Dispensers should be mounted carefully such that they have a line of sight access to the glass cuvette. Line of sight access is important because dispensers need to shoot the rubidium atoms inside the cell so that the loading process becomes successful. Additionally, the distance between the glass cuvette and dispensers should not be long in order to avoid the failed loading.

Figure 27: Rubidium dispensers fixed to the vacuum electrical feedthrough. Dispensers should be carefully mounted with respect to the direction of the gravity and should be carefully cleaned beforehand.

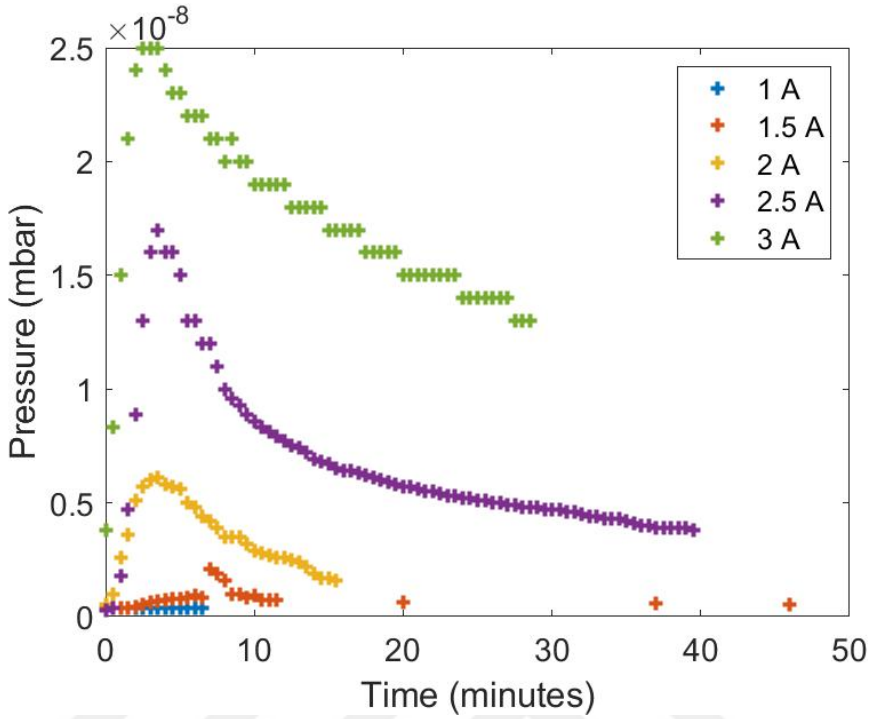

Figure 28: Graphs shows the relationship between rubidium dispensers' current and vacuum pressure. Higher the current applied, more atoms are released.

The rubidium dispenser used is selected in Type C. The shape of the dispenser and its connection to the electrical feedthrough pins are shown in Fig. 26 and Figure Fig. 27. Green connections shown in Fig. 26 demonstrate the correct way of mounting in terms of the direction of the gravity.

After the electrical feedthrough is plugged in and the baking process is done, various currents are given to the rubidium dispensers and the pressure change is observed. The rubidium dispenser has no polarity and can be supplied either way. These values are shown in the graph in Fig. 28.

After applying current to the rubidium dispensers, a probe laser is focused and directed to the vacuum glass cuvette. This is done to observe the Rb fluorescence from the glass cuvette to make sure that the loading is successful and that there are enough Rb atoms to use. No fluorescence is observed in any of the current values shown in the graph above. The fluorescence seen in Fig. 29 is observed when the current is set

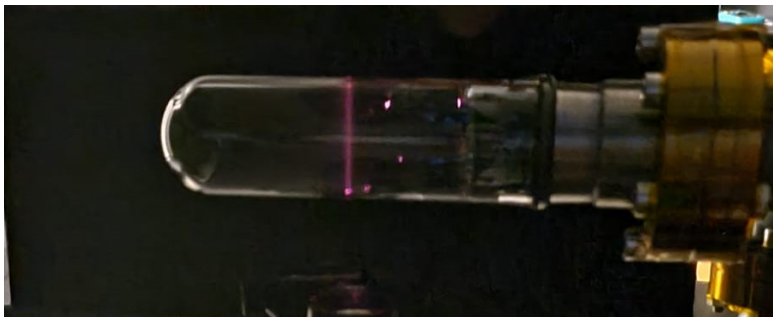

Figure 29: Image of ^{87}Rb fluorescence generated by a 780 nm narrowband laser passing vertically through a vacuum glass cuvette.

to 4.5 amps for testing purposes. Although two rubidium dispensers are attached to the system in these measurements, only one of them is used, and a spare dispenser is added in order not to open the ultra-high vacuum (UHV) assembly again in case the other one loses electrical contact or melts the Rubidium atom reserve. The reason why Rb fluorescence can be seen at a high current is that the atoms coming out of the Rb dispenser increases exponentially with the increasing current value.

In this experiment, it is encountered that the glass cuvette is painted blue at a certain polar angle due to the indium surface coating of the dispenser. During the first operation, indium coating is heated and vaporized through the air and condensate on the surface of the glass which can be seen in Fig. 30. In about 2 hours, most of the blue strip is cleaned with the help of the ion pump, and the vacuum system and rubidium dispenser become suitable to use again. The fact that this line is symmetrical with respect to the center of the glass cuvette confirms that the rubidium dispenser is fixed in the ideal geometry in the vacuum assembly and that the rubidium atoms are directed to the cuvette center where the MOT should be established.

4.6 Ion pump troubleshooting

After baking the whole setup and heating the rubidium dispensers, the total pressure of the vacuum chamber starts to fluctuate with the increasing trend. No potential outgassing and leakage source could be found. Since the valve that separates the turbo

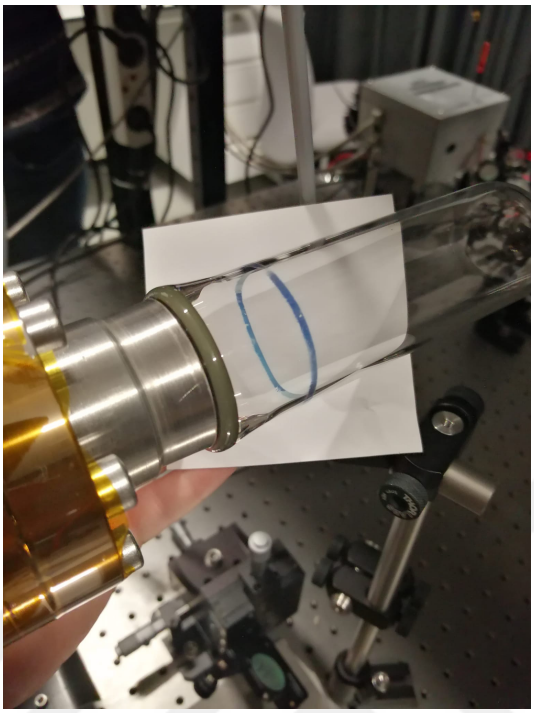

Figure 30: Residue formed by evaporated indium coating of the Rb dispenser. With the help of the ion pump, contaminants are quickly removed.

and the ion pump is closed, vacuum readings can only be done by the integral pressure gauge of the ion pump controller. The ion pump vacuum gauge infers information about the pressure values from the current reading between the electrodes. If the pressure is high, that means lots of gasses inside the chamber are ionized and captured by the ion pump electrodes resulting in the high electrode current. If the pressure is low inside the chamber, that results in a low electrode current inside the ion pump. Since the pressure measurements can be done only by the ion pump controller and its accuracy depend on the load and contamination in the electrodes, we suspect the reading might be inaccurate. After firing the rubidium dispensers, ion pump electrodes might be saturated and inaccurate vacuum reading caused by the stray current might be the reason for the pressure value change. In order to solve the problem, additional baking might be needed but before that, hi-potting can solve the issue. Hi-potting is the practice of applying over-voltage to the pump to get rid of any extraneous conducting material. Hi-potting is required when the current reading

is not proportional to the pressure reading of the pump controller. When the pump is old enough and has worked at high pressure for a long time, leakage is not coming from the cable or the controller, or when the leakage current is of the same order of magnitude as the pump, hi-potting is needed. It should be implemented carefully so that potential arcing inside the pump does not cause any problem. If arcing occurs, wait until the current is stable again. Applied voltage should be slowly increased and it should be constantly watched. Increase the applied voltage from 0 V to maximum voltage in 30 seconds and wait a maximum of 15 seconds in the highest voltage. The current value should not exceed 50 mA for our application. Max voltage values are 8 kV AC max or 11 kV DC max with standard cables.

CHAPTER V

NEAR-CONCENTRIC CAVITY SIMULATIONS FOR CAVITY QED EXPERIMENTS WITH COLD ATOMS

Recent experimental developments allow experimenters to isolate and manipulate the individual quantum systems with increased interaction strengths. One of the most important examples of this experimental ability is provided by the means of cavity QED. Experimental capabilities and applications of these devices are so diverse that it includes a study of quantum gases, precise control of atoms and molecules, and quantum networks [61, 62, 30, 63, 64, 65, 66, 32, 67]. All the applications listed above require a strong atom-photon coupling, high precision, and sensitivity which makes it crucial to know the mode structure of the optical cavity of interest [68, 69]. Within the cavity QED domain, near-concentric cavities are the usual solutions to reach the strong coupling regime. In a strong coupling regime, atom-cavity coupling which is represented by g_0 dominates the two dissipative rates, which are atomic decay rate (γ) and cavity damping rate ($\mathcal{K}$),

$$g_0 \gg \gamma, \mathcal{K} \tag{15}$$

The coupling coefficient can be written in terms of the scattering ratio as,

$$g_0 = \sqrt{\frac{\pi c R_{sc}(u)}{\tau L}} \tag{16}$$

where c is the speed of light in the vacuum, τ is the lifetime of the atom of interest, and L is the cavity length. The scattering ratio can be written as follows,

$$R_{sc}(u) = \frac{3}{4u^3} e^{2/u^2} \Big[\Gamma\Big(\frac{-1}{4}, \frac{1}{u^2}\Big) + u\Gamma\Big(\frac{1}{4}, \frac{1}{u^2}\Big) \Big]^2 \tag{17}$$

where u is the focusing parameter which is defined as the ratio of the input beam waist at the cavity mirrors to half of the cavity length L and Γ is the incomplete gamma

function. From the focusing parameter u, a requirement for the strong focusing cavity can be seen. The scattering ratio is formulized semi-classically which treats the atom as a quantum object whereas the light field is classical. For the complete treatment see Ref. [70, 4]. The near-concentric cavity, where the cavity length is twice the radius of curvature of the mirrors, has the strongest focusing mode and a cavity beam waist that can reach a diffraction limit of $\lambda/2$. However, high focusing strength comes with a price. Not all cavities are as stable as the other types and stability conditions are strict for the near-concentric case. For a stable cavity roughly two conditions should be met; the incident optical mode wavefront should match the cavity mirrors and mirrors should be placed at the node of the standing wave pattern. The stability diagram can be seen in Fig. 31. As can be seen from the graph, near-concentric cavities are at the edge of the stability diagram and naturally suffers from diffraction losses and optical aberrations. Aberrations distort the input mode and result in the excitation of the higher-order spatial transverse modes of the cavity.

In order to have a stable cavity, following condition should be met,

$$0 \leq g_1 g_2 \leq 1 \tag{18}$$

where $g_1 = 1 - \frac{L}{R_1}$ and $g_2 = 1 - \frac{L}{g_2}$. Here L is the cavity length and R_1 and R_2 are the radius of curvatures of the mirrors [71].

The frequency difference between two successive longitudinal cavity modes which is called a free spectral range (FSR) is defined as,

$$\nu_{FSR} = \frac{c}{2L} \tag{19}$$

where L is the cavity length and c is the speed of the light in the vacuum, as usual. The frequency difference between adjacent transverse higher-order cavity modes for $p, l > 0$ is written as [70],

$$\Delta\nu_{l,p} = \frac{c}{2\pi L} = (|l| + 2p) \arccos\left(1 - \frac{L}{R_m}\right) \tag{20}$$

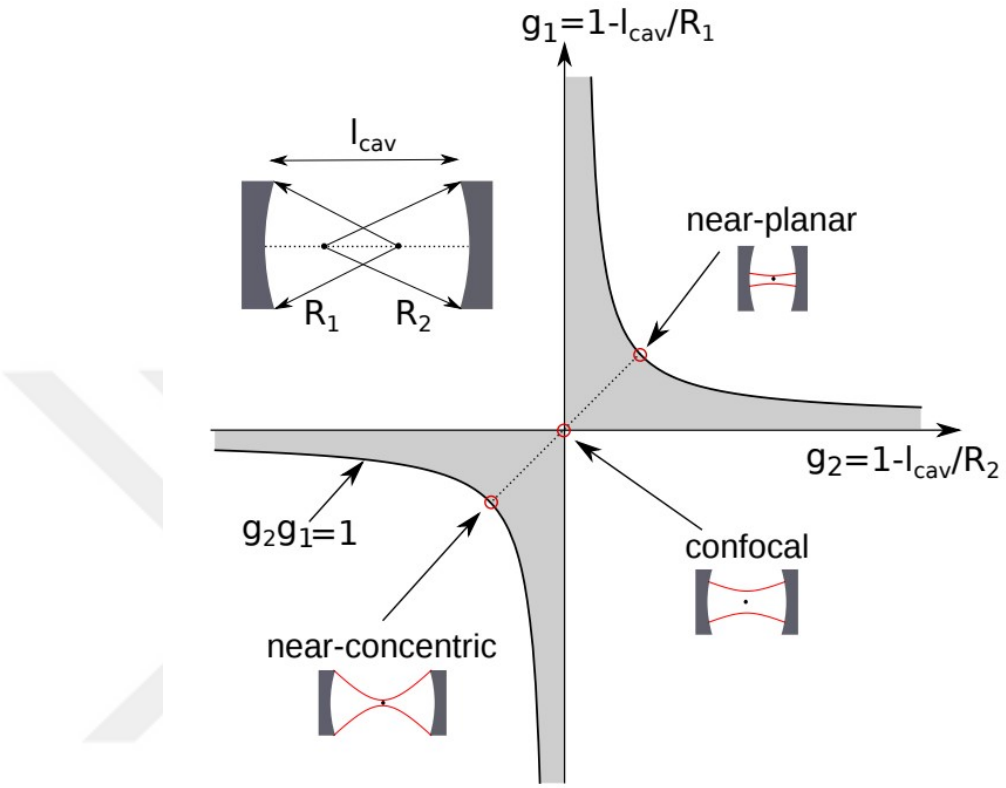

Figure 31: The stability diagram for optical cavities constructed with two mirrors [4].

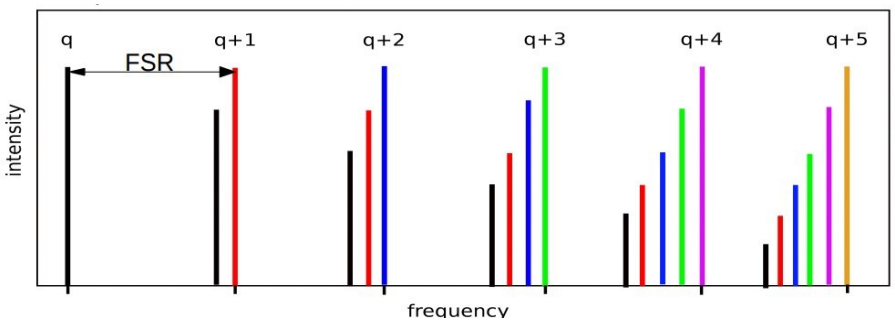

Figure 32: Transverse and longitudinal modes for near-concentric cavities. The FSR represents the frequency difference between two successive longitudinal modes.

For the exact confocal configuration where $L = R$, $\Delta\nu_{l,p}$ is equal to the half of the FSR, whereas for an exact concentric case where $L = 2R$, $\Delta\nu_{l,p}$ is equal to the FSR value. For a visualization see Fig. 32. Mode spacing in the frequency domain makes the higher-order modes in confocal cavities distinguishable, while the concentric cavities have closely spaced higher-order modes. When these closely spaced modes add up, it becomes impossible to differentiate the higher-order modes and contributes to the increase in the cavity linewidth. For the applications that require high precision, knowing the mode structure of the near-concentric cavities has vital importance for the apparent reasons. The simulation results of the near-concentric cavities for higher-order mode excitation and a comprehensive model for cavities with spherical mirrors is presented here.

5.1 Mathematical treatment

The physical system includes two spherical plano-concave mirrors whose mirror sizes (a), the radius of curvatures (ROC) and thicknesses (t) are taken as 6.35 mm, 50 mm, and 1.5 mm, respectively. 780 nm light is assumed since it corresponds to the D_2 line of the ^{87}Rb atom. Reflectivities are 0.9798 for both mirrors. Near-concentric cavity whose cavity length is nearly L = 100 mm is assumed. The physical system studied computationally can be seen in Fig. 33. For the complete treatment with the experimental verification see Ref. [72].

Since the cavity of interest has cylindrical symmetry, Laguerre-Gaussian modes are the appropriate set of solutions to describe the system. These set of polynomials are written as [71],

$$\begin{aligned}\Psi_{lp}(r,\phi,z) = C_{lp}\frac{w_0}{w(z)}\frac{r\sqrt{2}}{w(z)}^{|l|}\exp\Big(\frac{-r^2}{w(z)^2}\Big)L_p^{|l|}\Big(\frac{2r^2}{w(z)^2}\Big)\\ \times\exp\Big(\frac{ikr^2}{2R(z)}\Big)\exp\big(il\phi\big)\exp\big([-i(2p+|l|+1)\xi(z)]\big)\end{aligned} \tag{21}$$

where $L_p^{|l|}$ are generalized Laguerre polynomials, $w(z)$ is the beam waist, p and l are

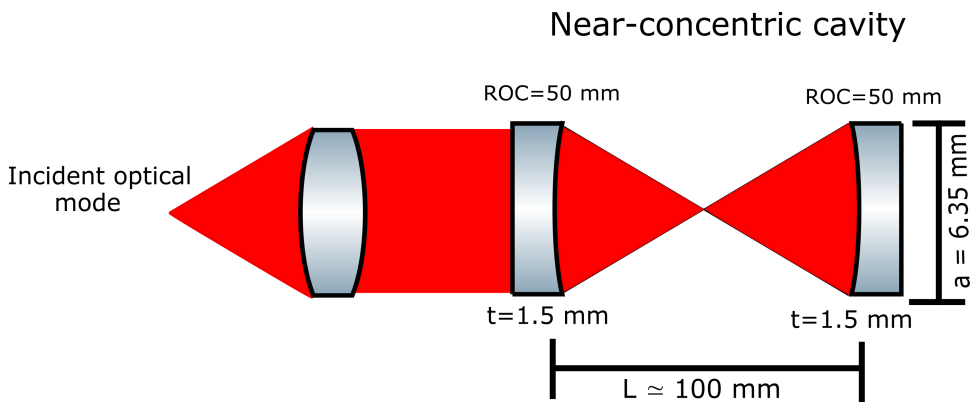

Figure 33: Diagram of the physical system assumed. Radius of curvature of the mirrors (ROC) are 50 mm, thickness is $t = 1.5$ mm, aperture size is $a = 6.35$ mm and cavity length is nearly $L = 100$ mm.

the radial and azimuthal indices, R(z) is the radius of curvature of the wavefront, $\xi(z)$ is the Gouy phase written in terms of the Rayleigh length, and C_{lp}'s are the normalization coefficients. Incident optical mode is the fundamental cavity eigenmode in the form of LG_{00} and is written as,

$$\Phi(r,\phi,z) = C_{00}\frac{w_0}{w(z)}\exp\Big(\frac{-r^2}{w(z)^2}\Big)\exp\Big(\frac{ikr^2}{2R(z)}\Big)\exp\Big(-i\xi(z)\Big). \tag{22}$$

$\xi(z)$ in the last term describes the phase profile of the input mode which is calculated by the ray-tracing methods in accordance with the real physical system described above [73, 74]. Phase retardation is introduced to the optical mode to describe the aberrations caused by the improper incident mode coupling. In order to find the cavity length and the beam waist at the mirror, start with the following equation,

$$R(z) = z\Big(1+\Big(\frac{\pi w_0^2 n}{\lambda z}\Big)^2\Big) \tag{23}$$

Finding the z value whose radius of curvature is exactly equal to the radius of curvature of the mirror gives the length of the cavity. By substituting the cavity length to below,

$$w(z) = w_0\Big(1+\Big(\frac{z}{z_0}\Big)^2\Big)^{1/2}. \tag{24}$$

beam waist at the mirror can be found. Coupling strength of the incident optical

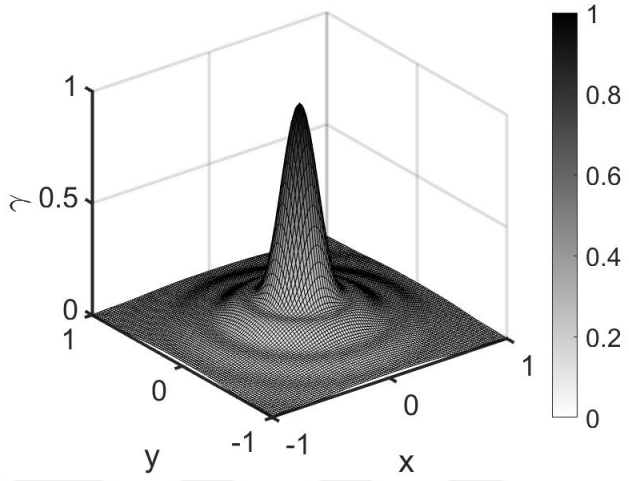

Figure 34: Overall cavity field plotted for the minimum beam waist of $w_0 = 7.3\,\mu$m. γ is the transmission inside the cavity, which is plotted spatially having x and y as the spatial axes.

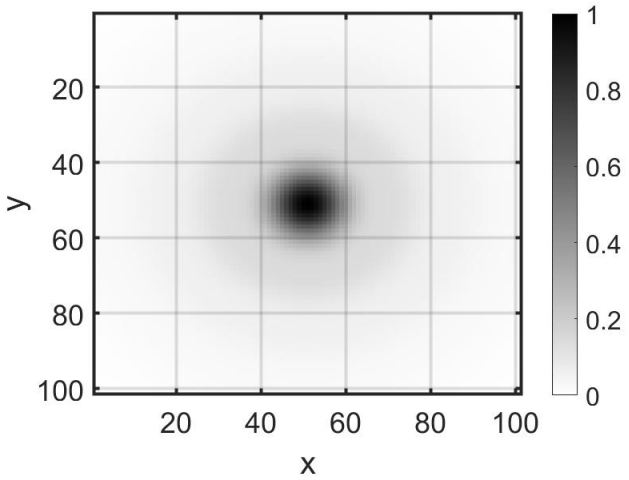

Figure 35: Heat map and the camera photograph showing the cavity field distribution for t"he minimum beam waist of $w_0 = 7.3\,\mu$m.

mode to each cavity eigenmode can be characterized by the overlap function,

$$\gamma_{lp} = |\Psi_{lp}(r,\phi,z)^{*}\Phi(r,\phi,z)|^{2}. \tag{25}$$

3D and heat map plots of the γ function can be seen in Fig. 34 and Fig. 35. Due to their various sizes, each cavity mode is affected differently by the diffraction losses. Since they are greater in size, higher-order modes are affected more. For each cavity eigenmode, power loss after one round trip due to the diffraction loss should be calculated individually and it is written as,

$$\alpha_{lp} = \left| \frac{\int_0^a \int_0^{2\pi} |\Psi_{lp}|^2 r dr d\phi}{\int_0^\infty \int_0^{2\pi} |\Psi_{lp}|^2 r dr d\phi} \right|^2 \tag{26}$$

where a is the size of the mirror aperture. The coefficient of finesse F_{lp} is defined as [75],

$$F_{lp} = \frac{4\rho_{lp}}{(1-\rho_{lp})^2} \tag{27}$$

Here, ρ_{lp} should be calculated individually for each higher-order mode and named as reflection coefficient. It can be written as,

$$\rho_{lp} = R_m^2 \Big(\int_0^a \int_0^{2\pi} |\Psi_{lp}(r,\phi,z)|^2 r dr d\phi \Big)^2. \tag{28}$$

By taking diffraction losses and reflection coefficients into account, the total cavity transmission for each higher-order mode can be calculated as [76],

$$T_{lp} = \alpha_{lp}\gamma_{lp} \frac{1}{1 + F\sin^2 \delta/2} \tag{29}$$

where δ is the phase difference between the interfering wavefronts and can be written as $\delta = 2\pi\omega L/c$. Using the coefficient of finesse, finesse itself can be written as in that case,

$$\mathcal{F}_{lp} = \frac{\pi}{2}\sqrt{F_{lp}}. \tag{30}$$

Finesse and the linewidth are the two faces of the same medal and they are inversely proportional to each other with a scale of an FSR.

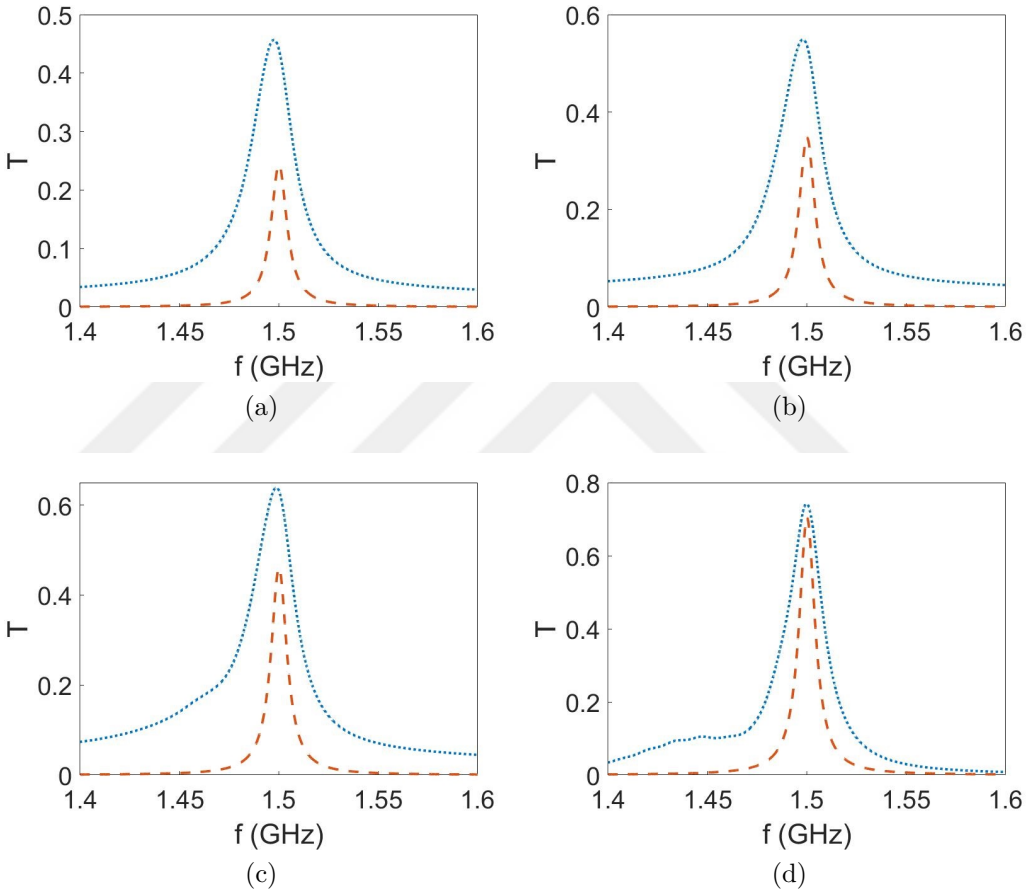

Figure 36: Total cavity transmission in the frequency domain. The dashed red curve shows the fundamental mode whereas the dotted blue curve shows the total cavity transmisison. Figures a) b) c) and d) demonstrate the cases where minimum beam waists are 5.7, 6.5, 7.3, and 9.3 μm, respectively. Total cavity linewidth values are $\kappa = 26.324, 27.868, 28.002$ and 22.175 MHz, respectively.

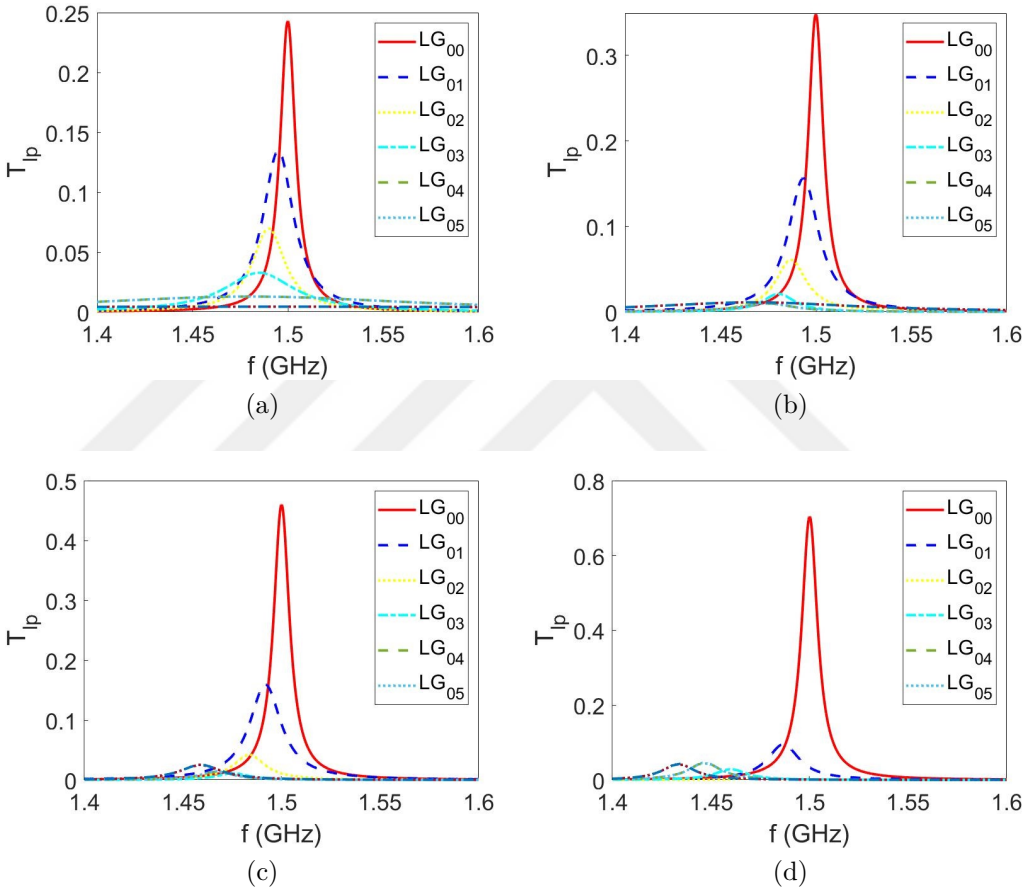

Figure 37: The transmission for each cavity eigenmode. The solid red curve is for the fundamental mode LG_{00}, the dashed blue curve is for the first higher-order mode LG_{01}, the dotted pink curve is for the LG_{02} mode and the dot-dashed cyan curve is for the LG_{03} mode. Figures a) b) c) and d) demonstrate the cases where minimum beam waists are 5.7, 6.5, 7.3, and 9.3 μm, respectively.

5.2 Mode decomposition analysis

Exact concentric cavities are not reachable due to diffraction. In order for the beam waist at the focus to be infinitesimal, mirror sizes should be infinite which is an unphysical case apparently. Generally, near-concentric cavities have few micrometer minimum beam waist sizes and to see the effect of the focusing strength four different minimum beam waist size cases are examined in this work. The minimum beam waist size range used in this work is between nearly $5 - 10$ μm. To be specific four different cases are examined which are $\omega_0 = 5.7, 6.5, 7.3$, and 9.3 μm. Since 780 nm light is used, 5.7 μm minimum beam waist size is physically a reasonable choice and it satisfies the strong focusing conditions. After 10 μm higher-order modes start to be separated and beyond that value, the linewidth broadening effect becomes insignificant.

T_{lp}'s represent the amount of transmission for each transverse higher-order mode inside the cavity, and it can be seen in Fig. 36 and Fig. 37 for four different minimum beam waist values. Fig. 36 shows the overall behavior whereas Fig. 37 shows the individual higher-order modes separately. From Fig. 37 it is seen that higher-order modes are closely spaced and they are impossible to resolve altogether. The final cavity transmission peak looks like a nice Gaussian shape and it is not possible to understand the mode composition of the final transmission curve. This effect is significant when the focusing strength of the cavity increases. Smaller minimum beam waist values are prone to be disturbed compared to the other cases. The linewidth broadening effect decreases with the increasing minimum beam waist as can be seen in Fig. 36 and Fig. 37, with exact linewidth values of $\kappa = 26.324, 27.868, 28.002$, and 22.175 MHz, respectively. For the minimum beam waist values of $\omega_0 = 5.7, 6.5$, 7.3 μm, linewidth values are comparable, unlike the considerable decrease for $\omega_0 = 9.3$ μm. Uncertainty in the mode structure makes the strong focusing cavities inappropriate for experiments that require high precision.

The coupling efficiency of each higher-order mode is defined as γ_{lp} and shown in

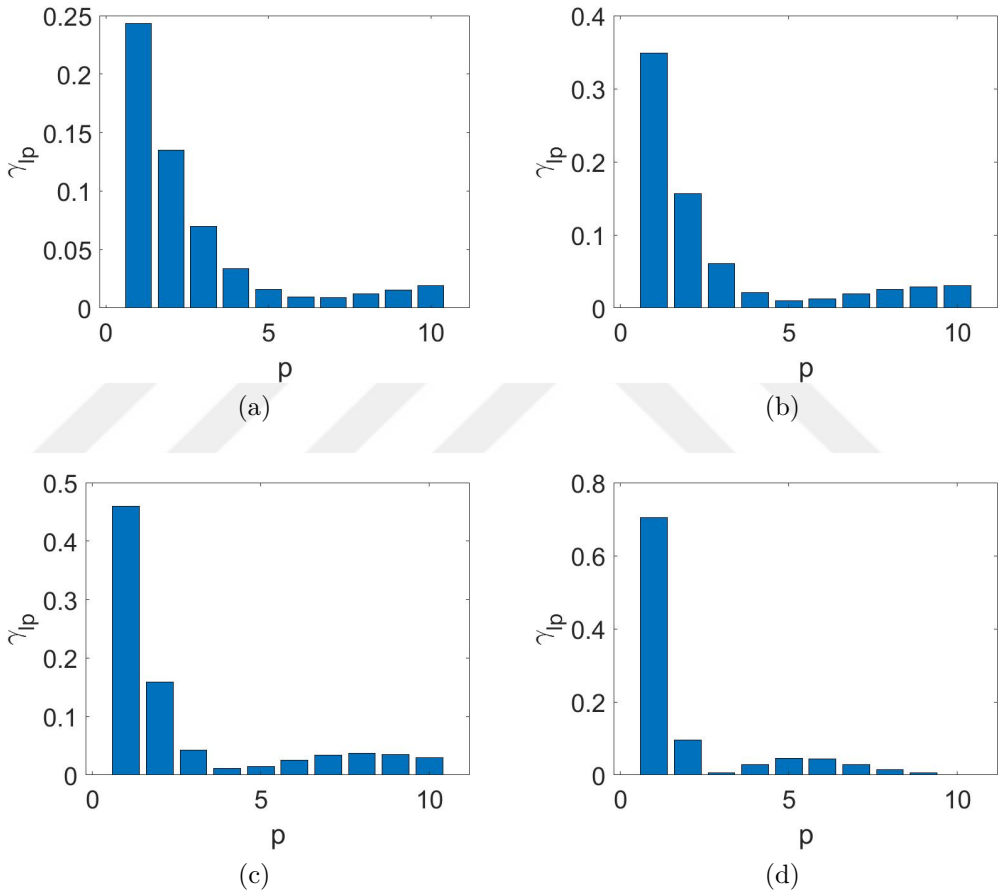

Figure 38: The overlap function γ_{lp} calculated for the optical mode and each cavity mode LG_{lp}. Figures a) b) c) and d) demonstrate the cases where minimum beam waists are 5.7, 6.5, 7.3, and 9.3 μm, respectively.

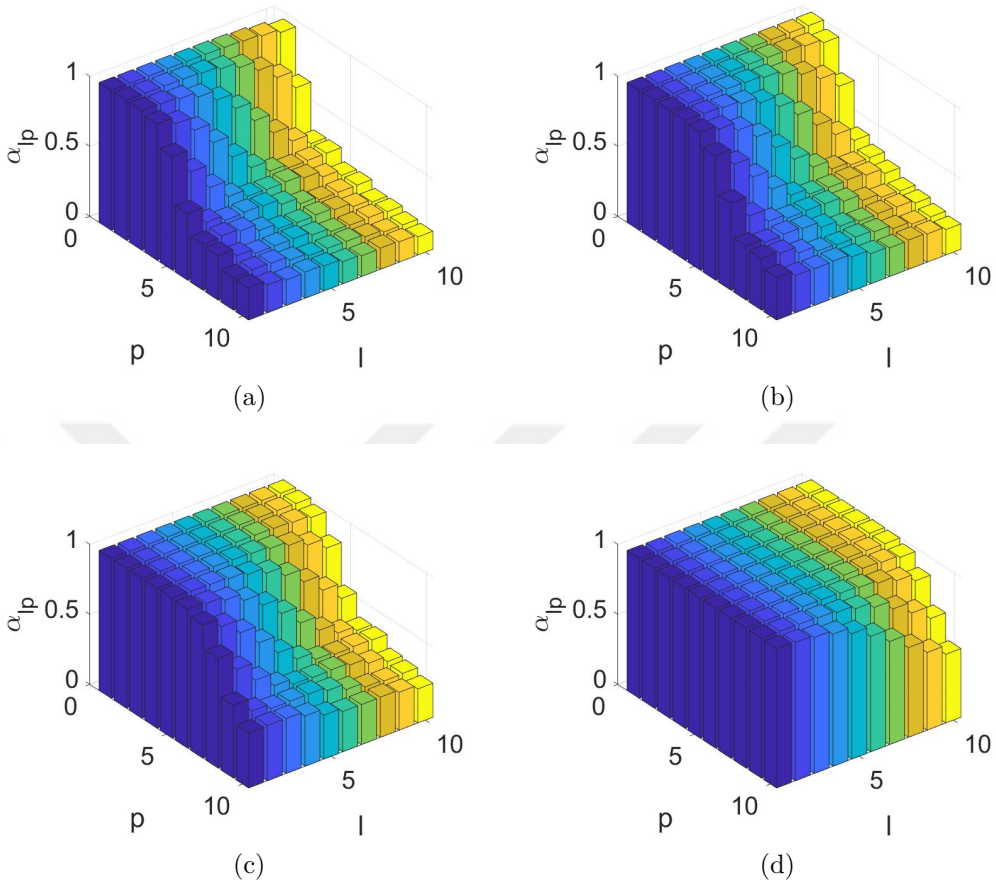

Figure 39: Power left (α_{lp}) in each cavity mode (LG_{lp}) after one round trip for different azimuthal and radial mode indices l and p values. Figures a) b) c) and d) demonstrate the cases where minimum beam waist values are 5.7, 6.5, 7.3, and 9.3 μm, respectively.

Fig. 38 for four different minimum beam waists $\omega_0 = 5.7, 6.5, 7.3$, and 9.3 μm. From the figure, it is seen that only radial modes are excited since the phase of the optical mode is degraded in the radial direction. Coupling efficiencies are minimized after the first several fundamental modes which show that the effect is significant for this regime. Furthermore, as expected, with the increasing minimum beam waist, coupling efficiencies decrease for the higher-order modes.

One of the most important factors that affect cavity transmission is the diffraction losses. Due to their different spatial distribution, each higher-order mode is affected differently by the size of the mirrors. Since the higher-order modes are larger, they

are affected by the diffraction losses more. After one round trip, power left inside the cavity for each higher-order mode can be seen in Fig. 39 for again four different minimum beam waists $\omega_0 = 5.7, 6.5, 7.3$, and 9.3 μm. For larger minimum beam waist sizes, the effect of the diffraction losses becomes minimized due to the decreasing focusing strength. When the minimum beam waist size increases, the size of the beam waist at the mirror decreases which results in the smaller transverse field distribution of the cavity modes.

Even if the effect of the aperture size is revealed in the effect of diffraction losses, it might be intuitive to dig deep into this issue and see the effect of the increasing aperture size on the linewidth of each higher-order mode which can be seen in Fig. 40 for four different minimum beam waists. With the increasing aperture size, linewidth for each cavity eigenmode decreases. The trend is similar for different minimum beam waist values although the decrease is sharper for greater minimum beam waist cases. As the mirror size increases, the effect of diffraction losses becomes insignificant, and as a result, linewidth decreases.

The last parameter that is discussed in this context is the reflectivity of mirrors. Again the effect of the reflectivity differs for each higher-order mode and changes for different minimum beam waist cases. The effect of the reflectivity on the first few cavity modes can be seen in Fig. 41. For the calculation, not only the bare reflectivity value is taken into account but also reflectivity affected by the diffraction losses is calculated which can be written as $R_{\text{eff}} = \rho R$. For greater minimum beam waist sizes, the effect of the reflectivity is similar. With the increasing reflectivity, each higher-order mode will have lower linewidth and overall cavity behavior is improved.

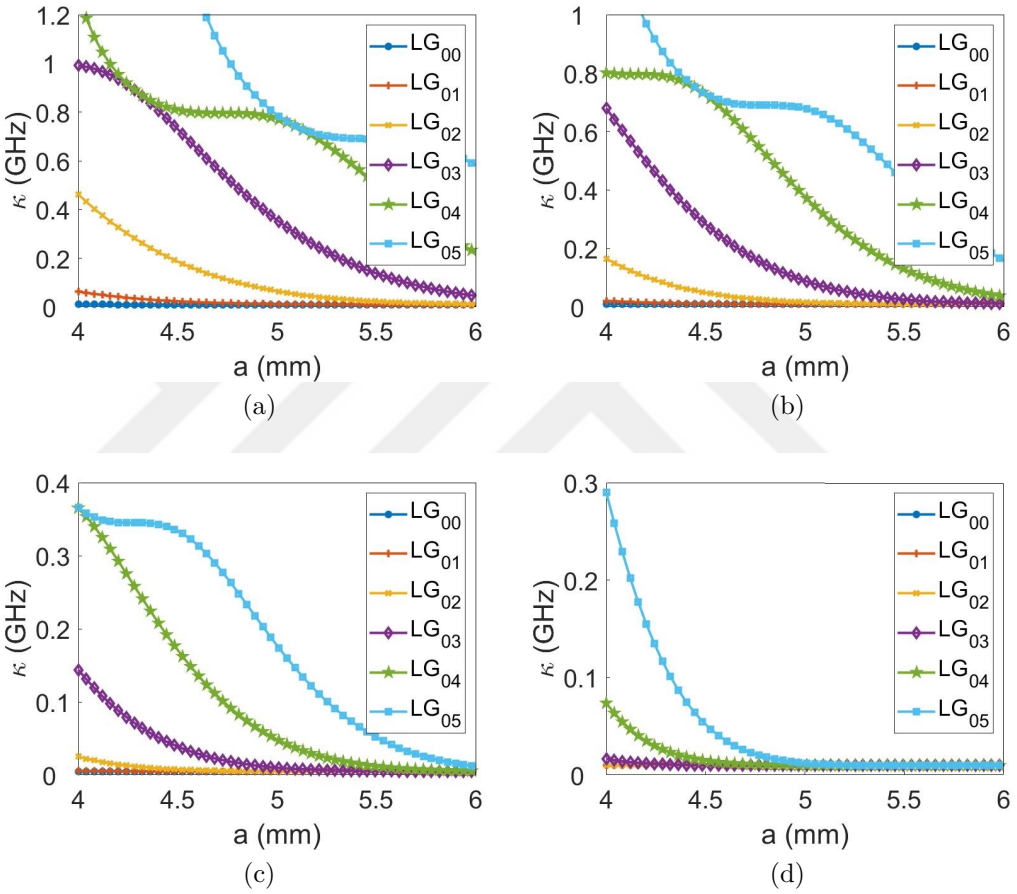

Figure 40: Change in the linewidth of the each higher-order mode LG_{lp} with the changing aperture size (a). The circle marker blue curve is for the fundamental mode LG_{00}, the rectangular marker orange curve is for the first higher-order mode LG_{01}, the cross marker yellow curve is for the LG_{02} mode and the diamond marker purple curve is for the LG_{03} mode. κ is the linewidth in the units of GHz and a is the aperture size in the units of mm.

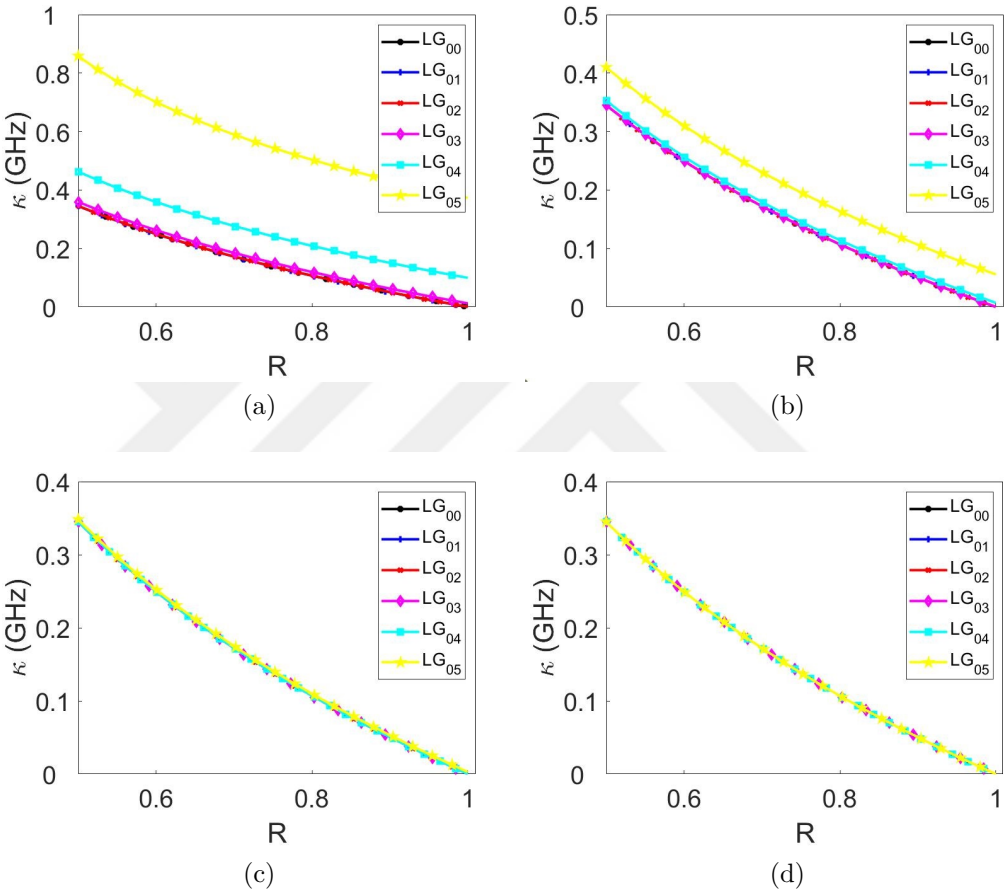

Figure 41: Change in the linewidth of the each higher-order mode by changing effective mirror reflectivity. Figures a) b) c) and d) demonstrate the cases where minimum beam waists are 5.7, 6.5, 7.3, and 9.3 μm, respectively. The circle marker black curve is for the fundamental mode LG_{00}, the rectangular marker blue curve is for the first higher-order mode LG_{01}, the cross marker red curve is for the LG_{02} mode and the diamond marker purple curve is for the LG_{03} mode. κ is the linewidth in the units of GHz and R is the reflectivity given in the range of 0-1.

CHAPTER VI

CONCLUSION

In this thesis, preliminary processes and setups for the single atom experiments are presented and explained. Experiments with single atoms offer a wide range of scientific and engineering applications. Fundamental physical phenomena can be investigated and measurements that require high precision can be done. To perform single atom experiments magneto-optical trap should jointly be used with the optical dipole trap. Fundamental laser and vacuum setups are constructed and results are presented. These setups, which are ECDL and FM Spectroscopy, are required to address the desired atomic transition with the required precision and accuracy. ^{87}Rb D_1 and D_2 line transitions are successfully scanned and traced. Each Rb hyperfine transitions in the D_2 line can be identified and used for further experimentation. Even though the PID controller is ready to operate, the error signal required to lock the laser frequency to the specific frequency cannot be achieved due to combined noise coming from the experimental devices. Alongside the laser setups, ultra-high vacuum apparatus is constructed and with the help of the baking and careful vacuum design and handling, a final pressure value of 2.5×10^{-10} mbar is achieved, which is sufficient enough for the applications planned to be performed. Rb dispensers that are used as a Rb atom source are explained in detail and mounted. Rb loading to the glass cuvette from this source is performed successfully. In addition to the experimental progress explained here, near-concentric cavity simulations are performed and the model used for these calculations is explained in detail. The model is so general that it can be used to analyze the cavities which are constructed by two spherical mirrors. With the defined model, few decisive cavity parameters are investigated and the effect of higher-order

mode excitation is studied by using the mode decomposition analysis. From the analysis, it becomes obvious that the effect of higher-order mode excitation is decisive for the strong focusing cavities.

APPENDIX A

NOTES ON BAKING

- Baking is needed to effectively remove water vapor and reduce hydrogen.
- Baking does not remove hydrocarbons which should be avoided, since they might crack and burn into the chamber surface.
- With baking, results become better with time linearly and with temperature exponentially.
- Minimum temperature values for each vacuum chamber element should be noted and temperature should be carefully increased.
- Heating must be even for all surfaces except the exhaust part which is the turbo pump. Turbo pump temperature should be slightly lower.
- Best to start baking with ion pump off; use turbo pump to remove gas first.
- Best results are obtained if the system is pumped down to the base pressure before baking starts. Pump down to 10-4 or 10-5 mbar at least with turbo pump.
- Best if each pump is processed following its own outgassing rate "pressure-control" is important, not time-control".
- After the bake-out curve approaches flat, the ion pump can be started.
- Check the maximum current of the ion pump and make sure that it doesn't exceed the maximum baking current and eventually switch off the heating.
- Don't forget to outgas filaments (not at room temperature).

- When the ion pump reaches full voltage and stable current, close the valve and turn off the heat.
- Allow the system to reach base pressure.
- Venting with dry nitrogen will help to gain a good vacuum before baking!

APPENDIX B

ADDITIONAL IMAGES

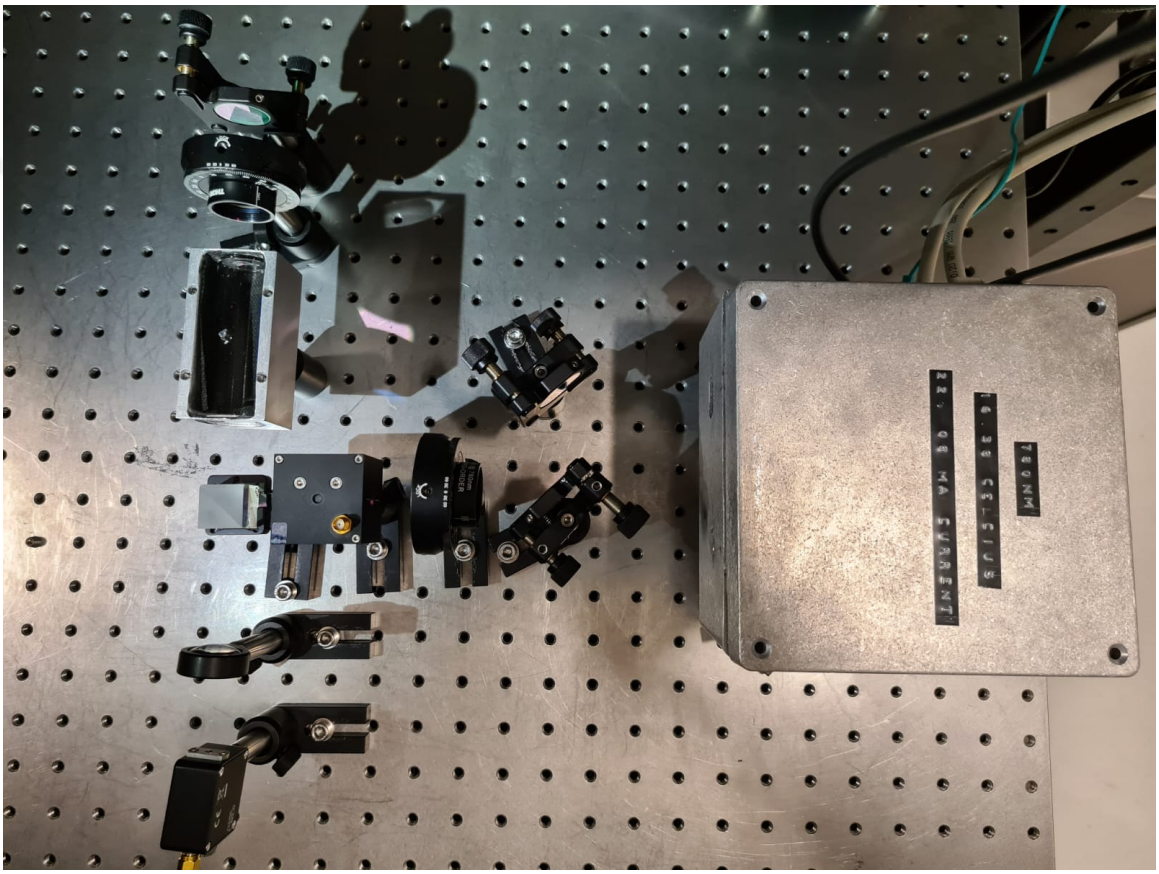

Figure 42: Image of the laser setup shown from the top view.

Figure 43: Wires in a cardboard. Cardboards are then wrapped around the vacuum setup.

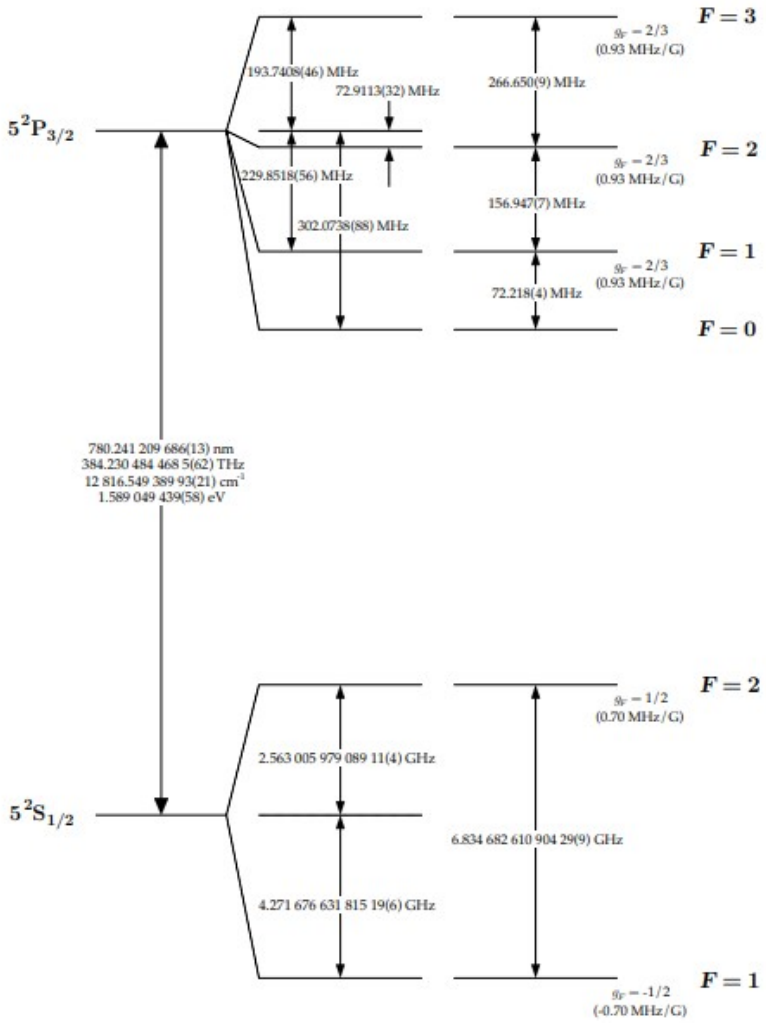

Figure 44: ^{87}Rb D_2 line hyperfine structure. Different energy levels of ^{87}Rb can be seen. Taken from Ref. [5]

.

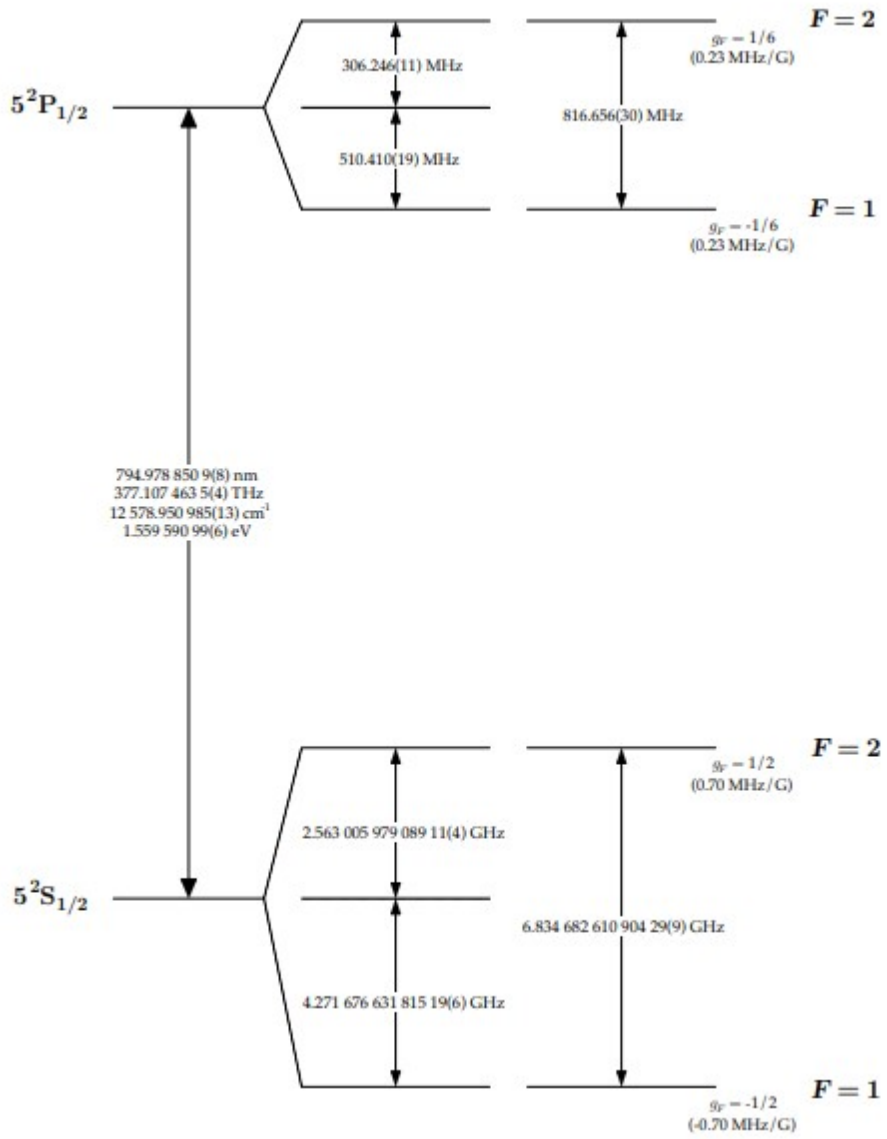

Figure 45: ^{87}Rb D_1 line hyperfine structure. Different energy levels of ^{87}Rb can be seen. Taken from Ref. [5]

.

Bibliography

[1] Thorlabs, "Near-ir ruled reflective gratings." https://www.thorlabs.com/newgrouppage9.cfm?objectgroup_id=8627, June 2022.

[2] Moglabs, "Dlc performance." https://www.moglabs.com/support/performance, June 2022.

[3] Alfavakuo, "Dispenser dimensions." https://alfavakuo.eu/products/mvs/dimensions, June 2022.

[4] N. C. Huan, *Single Atoms Coupled to a Near-Concentric Cavity*. PhD thesis, National University of Singapore (Singapore), 2018.

[5] D. A. Steck, "Rubidium 87 d line data," 2001.

[6] T. H. Maiman, T. H. Maiman, and Holland, *Laser Inventor*. Springer, 2018.

[7] T. W. Hänsch and A. L. Schawlow, "Cooling of gases by laser radiation," *Optics Communications*, vol. 13, no. 1, pp. 68–69, 1975.

[8] S. Chu, L. Hollberg, J. E. Bjorkholm, A. Cable, and A. Ashkin, "Three-dimensional viscous confinement and cooling of atoms by resonance radiation pressure," *Physical Review Letters*, vol. 55, no. 1, p. 48, 1985.

[9] S. Chu, J. Bjorkholm, A. Ashkin, and A. Cable, "Experimental observation of optically trapped atoms," *Physical Review Letters*, vol. 57, no. 3, p. 314, 1986.

[10] P. D. Lett, R. N. Watts, C. I. Westbrook, W. D. Phillips, P. L. Gould, and H. J. Metcalf, "Observation of atoms laser cooled below the doppler limit," *Physical Review Letters*, vol. 61, no. 2, p. 169, 1988.

[11] A. Aspect, E. Arimondo, R. e. a. Kaiser, N. Vansteenkiste, and C. Cohen-Tannoudji, "Laser cooling below the one-photon recoil energy by velocity-selective coherent population trapping," *Physical Review Letters*, vol. 61, no. 7, p. 826, 1988.

[12] C. Monroe, W. Swann, H. Robinson, and C. Wieman, "Very cold trapped atoms in a vapor cell," *Physical Review Letters*, vol. 65, no. 13, p. 1571, 1990.

[13] C. Salomon, J. Dalibard, W. Phillips, A. Clairon, and S. Guellati, "Laser cooling of cesium atoms below 3 μk," *EPL (Europhysics Letters)*, vol. 12, no. 8, p. 683, 1990.

[14] A. Kastberg, W. D. Phillips, S. Rolston, R. Spreeuw, and P. S. Jessen, "Adiabatic cooling of cesium to 700 nk in an optical lattice," *Physical Review Letters*, vol. 74, no. 9, p. 1542, 1995.

[15] J. Reichel, F. Bardou, M. B. Dahan, E. Peik, S. Rand, C. Salomon, and C. Cohen-Tannoudji, "Raman cooling of cesium below 3 nk: new approach inspired by lévy flight statistics," *Physical Review Letters*, vol. 75, no. 25, p. 4575, 1995.

[16] S. A. Aljunid, G. Maslennikov, Y. Wang, H. L. Dao, V. Scarani, and C. Kurtsiefer, "Excitation of a single atom with exponentially rising light pulses," *Physical Review Letters*, vol. 111, no. 10, p. 103001, 2013.

[17] R. Gutzler, M. Garg, C. R. Ast, K. Kuhnke, and K. Kern, "Light–matter interaction at atomic scales," *Nature Reviews Physics*, vol. 3, no. 6, pp. 441–453, 2021.

[18] A. M. Kaufman and K.-K. Ni, "Quantum science with optical tweezer arrays of ultracold atoms and molecules," *Nature Physics*, vol. 17, no. 12, pp. 1324–1333, 2021.

[19] D. E. Chang, V. Vuletić, and M. D. Lukin, "Quantum nonlinear optics—photon by photon," *Nature Photonics*, vol. 8, no. 9, pp. 685–694, 2014.

[20] H. J. Kimble, "The quantum internet," *Nature*, vol. 453, no. 7198, pp. 1023–1030, 2008.

[21] S. Ebadi, T. T. Wang, H. Levine, A. Keesling, G. Semeghini, A. Omran, D. Bluvstein, R. Samajdar, H. Pichler, W. W. Ho, *et al.*, "Quantum phases of matter on a 256-atom programmable quantum simulator," *Nature*, vol. 595, no. 7866, pp. 227–232, 2021.

[22] D. Jaksch, J. I. Cirac, P. Zoller, S. L. Rolston, R. Côté, and M. D. Lukin, "Fast quantum gates for neutral atoms," *Physical Review Letters*, vol. 85, no. 10, p. 2208, 2000.

[23] A. Reiserer, N. Kalb, G. Rempe, and S. Ritter, "A quantum gate between a flying optical photon and a single trapped atom," *Nature*, vol. 508, no. 7495, pp. 237–240, 2014.

[24] L. Isenhower, E. Urban, X. Zhang, A. Gill, T. Henage, T. A. Johnson, T. Walker, and M. Saffman, "Demonstration of a neutral atom controlled-not quantum gate," *Physical Review Letters*, vol. 104, no. 1, p. 010503, 2010.

[25] H. J. Metcalf and P. van der Straten, *Laser Cooling and Trapping*. Springer-Verlag, 1999.

[26] R. Grimm, M. Weidemüller, and Y. B. Ovchinnikov, "Optical dipole traps for neutral atoms," in *Advances in Atomic, Molecular, and Optical Physics*, vol. 42, pp. 95–170, Elsevier, 2000.

[27] W. Demtröder, *Laser spectroscopy: vol. 2: experimental techniques*, vol. 2. Springer Science & Business Media, 2008.

[28] W. Demtröder, *Laser spectroscopy 1: basic principles*. Springer, 2014.

[29] R. Drever, J. L. Hall, F. Kowalski, J. Hough, G. Ford, A. Munley, and H. Ward, "Laser phase and frequency stabilization using an optical resonator," *Applied Physics B*, vol. 31, no. 2, pp. 97–105, 1983.

[30] C. Hood, M. Chapman, T. Lynn, and H. Kimble, "Real-time cavity qed with single atoms," *Physical Review Letters*, vol. 80, no. 19, p. 4157, 1998.

[31] C. J. Hood, T. Lynn, A. Doherty, A. Parkins, and H. Kimble, "The atom-cavity microscope: Single atoms bound in orbit by single photons," *Science*, vol. 287, no. 5457, pp. 1447–1453, 2000.

[32] C. H. Nguyen, A. N. Utama, N. Lewty, K. Durak, G. Maslennikov, S. Straupe, M. Steiner, and C. Kurtsiefer, "Single atoms coupled to a near-concentric cavity," *Physical Review A*, vol. 96, no. 3, p. 031802, 2017.

[33] F. Mivehvar, F. Piazza, T. Donner, and H. Ritsch, "Cavity qed with quantum gases: new paradigms in many-body physics," *Advances in Physics*, vol. 70, no. 1, pp. 1–153, 2021.

[34] C. Foot, "Atomic physics," *Oxford Master Series in Atomic, Optical and Laser Physics*, vol. 5, p. 134, 2005.

[35] C. Wieman, G. Flowers, and S. Gilbert, "Inexpensive laser cooling and trapping experiment for undergraduate laboratories," *American Journal of Physics*, vol. 63, no. 4, pp. 317–330, 1995.

[36] P. D. Lett, W. D. Phillips, S. Rolston, C. E. Tanner, R. Watts, and C. Westbrook, "Optical molasses," *JOSA B*, vol. 6, no. 11, pp. 2084–2107, 1989.

[37] S. Du, S. Zhang, Z. Shuyu, G. Y. Yin, and C. Belthangady, "Two-dimensional magneto-optical trap for neutral atoms," Sept. 16 2014. US Patent 8,835,833.

[38] C. E. Wieman and L. Hollberg, "Using diode lasers for atomic physics," *Review of Scientific Instruments*, vol. 62, no. 1, pp. 1–20, 1991.

[39] L. Ricci, M. Weidemüller, T. Esslinger, A. Hemmerich, C. Zimmermann, V. Vuletic, W. König, and T. W. Hänsch, "A compact grating-stabilized diode laser system for atomic physics," *Optics Communications*, vol. 117, no. 5-6, pp. 541–549, 1995.

[40] A. Arnold, J. Wilson, and M. Boshier, "A simple extended-cavity diode laser," *Review of Scientific Instruments*, vol. 69, no. 3, pp. 1236–1239, 1998.

[41] K. MacAdam, A. Steinbach, and C. Wieman, "A narrow-band tunable diode laser system with grating feedback, and a saturated absorption spectrometer for cs and rb," *American Journal of Physics*, vol. 60, no. 12, pp. 1098–1111, 1992.

[42] G. P. Nyamuda, "Design and development of an external cavity diode laser for laser cooling and spectroscopy applications," Master's thesis, Stellenbosch University (South Africa), 2006.

[43] R. Conroy, A. Carleton, A. Carruthers, B. Sinclair, C. Rae, and K. Dholakia, "A visible extended cavity diode laser for the undergraduate laboratory," *American Journal of Physics*, vol. 68, no. 10, pp. 925–931, 2000.

[44] S. D. Saliba, M. Junker, L. D. Turner, and R. E. Scholten, "Mode stability of external cavity diode lasers," *Applied Optics*, vol. 48, no. 35, pp. 6692–6700, 2009.

[45] Y. Zhao, J. Zhang, J. Stuhler, G. Schuricht, F. Lison, Z. Lu, and L. Wang, "Sub-hertz frequency stabilization of a commercial diode laser," *Optics Communications*, vol. 283, no. 23, pp. 4696–4700, 2010.

[46] T. Okoshi, K. Kikuchi, and A. Nakayama, "Novel method for high resolution measurement of laser output spectrum," *Electronics Letters*, vol. 16, no. 16, pp. 630–631, 1980.

[47] C. Petridis, I. Lindsay, D. Stothard, and M. Ebrahimzadeh, "Mode-hop-free tuning over 80 ghz of an extended cavity diode laser without antireflection coating," *Review of Scientific Instruments*, vol. 72, no. 10, pp. 3811–3815, 2001.

[48] D. McCarron, S. King, and S. Cornish, "Modulation transfer spectroscopy in atomic rubidium," *Measurement Science and Technology*, vol. 19, no. 10, p. 105601, 2008.

[49] J. Zhang, D. Wei, C. Xie, and K. Peng, "Characteristics of absorption and dispersion for rubidium d 2 lines with the modulation transfer spectrum," *Optics Express*, vol. 11, no. 11, pp. 1338–1344, 2003.

[50] J. H. Shirley, "Modulation transfer processes in optical heterodyne saturation spectroscopy," *Optics Letters*, vol. 7, no. 11, pp. 537–539, 1982.

[51] G. C. Bjorklund, M. Levenson, W. Lenth, and C. Ortiz, "Frequency modulation (fm) spectroscopy," *Applied Physics B*, vol. 32, no. 3, pp. 145–152, 1983.

[52] M. Gehrtz, G. C. Bjorklund, and E. A. Whittaker, "Quantum-limited laser frequency-modulation spectroscopy," *JOSA B*, vol. 2, no. 9, pp. 1510–1526, 1985.

[53] S. Nakanishi, H. Ariki, H. Itoh, and K. Kondo, "Frequency-modulation spectroscopy of rubidium atoms with an algaas diode laser," *Optics Letters*, vol. 12, no. 11, pp. 864–866, 1987.

[54] A. E. Domínguez, W. E. O. Larcher, and C. N. Kozameh, "Fundamental residual amplitude modulation in electro-optic modulators," *arXiv preprint arXiv:1710.10719*, 2017.

[55] C. J. Cuneo, J. J. Maki, and D. McIntyre, "Optically stabilized diode laser using high-contrast saturated absorption," *Applied Physics Letters*, vol. 64, no. 20, pp. 2625–2627, 1994.

[56] D. W. Preston, "Doppler-free saturated absorption: Laser spectroscopy," *American Journal of Physics*, vol. 64, no. 11, pp. 1432–1436, 1996.

[57] S. A. B. R. Aljunid, *Interaction of a strongly focused light beam with single atoms*. PhD thesis, National University of Singapore (Singapore), 2012.

[58] J. F. O'Hanlon, *A user's guide to vacuum technology*. John Wiley & Sons, 2005.

[59] P. Arciszewski, *An experimental apparatus for laser cooling of potassium and caesium*. PhD thesis, University of Warsaw Warsaw (Poland), 2019.

[60] G. Rayner, "Preparing a vacuum chamber to trap atoms, and the principles of a magneto-optical trap," 2010.

[61] S. M. Dutra, *Cavity quantum electrodynamics: the strange theory of light in a box*. John Wiley & Sons, 2005.

[62] R. Thompson, G. Rempe, and H. Kimble, "Observation of normal-mode splitting for an atom in an optical cavity," *Physical Review Letters*, vol. 68, no. 8, p. 1132, 1992.

[63] T. Puppe, P. Maunz, T. Fischer, P. W. Pinkse, and G. Rempe, "Single-atom trajectories in higher-order transverse modes of a high-finesse optical cavity," *Physica Scripta*, vol. 2004, no. T112, p. 7, 2004.

[64] A. Reiserer and G. Rempe, "Cavity-based quantum networks with single atoms and optical photons," *Reviews of Modern Physics*, vol. 87, no. 4, p. 1379, 2015.

[65] F. Brennecke, T. Donner, S. Ritter, T. Bourdel, M. Köhl, and T. Esslinger, "Cavity qed with a bose–einstein condensate," *Nature*, vol. 450, no. 7167, pp. 268–271, 2007.

[66] M. Clifford, J. Arlt, J. Courtial, and K. Dholakia, "High-order laguerre–gaussian laser modes for studies of cold atoms," *Optics Communications*, vol. 156, no. 4-6, pp. 300–306, 1998.

[67] C. H. Nguyen, A. N. Utama, N. Lewty, and C. Kurtsiefer, "Operating a near-concentric cavity at the last stable resonance," *Physical Review A*, vol. 98, no. 6, p. 063833, 2018.

[68] C. Bond, P. Fulda, L. Carbone, K. Kokeyama, and A. Freise, "Higher order laguerre-gauss mode degeneracy in realistic, high finesse cavities," *Physical Review D*, vol. 84, no. 10, p. 102002, 2011.

[69] A. N. Utama, C. H. Chow, C. H. Nguyen, and C. Kurtsiefer, "Coupling light to higher order transverse modes of a near-concentric optical cavity," *Optics Express*, vol. 29, no. 6, pp. 8130–8141, 2021.

[70] K. Durak, *A Diffraction Limited Fabry-Perot Cavity with a Strongly Focused Mode*. PhD thesis, National University of Singapore (Singapore), 2014.

[71] A. E. Siegman, *Lasers*. University Science Books, 1986.

[72] M. Öncü, M. Izadyari, Ö. E. Müstecaplıoğlu, and K. Durak, "A computational and experimental analysis of higher order modes in a strongly focusing optical cavity," *arXiv preprint arXiv:2205.14435*, 2022.

[73] K. Durak, C. H. Nguyen, V. Leong, S. Straupe, and C. Kurtsiefer, "Diffraction-limited fabry–perot cavity in the near concentric regime," *New Journal of Physics*, vol. 16, no. 10, p. 103002, 2014.

[74] D. Kleckner, W. T. Irvine, S. S. Oemrawsingh, and D. Bouwmeester, "Diffraction-limited high-finesse optical cavities," *Physical Review A*, vol. 81, no. 4, p. 043814, 2010.

[75] A. Yariv and P. Yeh, *Photonics: optical electronics in modern communications*. Oxford University Press, 2007.

[76] A. Lipson, S. G. Lipson, and H. Lipson, *Optical physics*. Cambridge University Press, 2010.

VITA

Mehmet Öncü is a member of Dr. Durak's Quantum Optics Laboratory (QOptics) team since 2020. He has received his bachelor's degree from the Physics Department at Bilkent University in 2020. He started his Masters' program with Dr. Durak in the same year. From the start of his Masters' program, he has been working in the project named Increasing Single Atom-Single Photon Interaction for Quantum Computing Applications funded by Scientific and Technological Research Council of Turkey (Tübitak) with the project number of 119F200. His research interest is on quantum optics and atomic physics in broad term. His masters' thesis focuses on the design and construction of the fundamental tools for atomic physics experiments.